

RC: Referee comment; **AR:** author's response; **AC:** author's changes in manuscript.

Referee #2 response

RC: This work applied the method of Broullón et al. (2019) to TCO₂ and extended the NN model by including year as an input and including TCO₂ computed from LDEO pCO₂ in the target. The manuscript is clearly written except for a few elements that require clarification; and the climatology TCO₂ data are useful for other modelers.

AR: Thank you so much for the thorough revision of the manuscript. We are pleased to see that you find the climatology useful for modelers. We hope to clarify your comments with the answers we give in this document and improve the manuscript. At the end of the answers, the new version of the manuscript is attached for a global view. We have tried to keep a balance to respond appropriately to the 3 reviewers.

RC: While including LDEO is expected to improve modeling TCO₂ dependence on input variables in the surface waters, it raises two questions. The first is the increase of the spatially biased sampling, which could lead to model optimization more weighted toward fitting the surface measurements.

AR: The inclusion of the variable depth as a predictor and its relevance in the computed TCO₂ (see Fig. S2) overcome this possible problem, otherwise errors below the surface (see Table 2) would be considerably higher than the measurement uncertainty in Gv2 (4 $\mu\text{mol kg}^{-1}$ for TCO₂; Olsen et al., 2016).

RC: The second is the unknown system bias of the computed TCO₂ relative to GLODAPv2 TCO₂. This bias could be estimated if there were enough overlapped points within the space and time resolutions of the training data. If you do the regression of Fig.2a using only the surface data, you may detect the bias. As the regression slopes of Fig.2a and 2b are 1, subtraction of the two predictions indicates the system bias of computed LDEO TCO₂. You mentioned on line 280 that “Interestingly, CANYON-B is able to reproduce the TCO₂ data derived from the complete LDEO dataset with a lower error than the one it obtains for the complete Gv2QC dataset in the surface ocean...”.

Another explanation to this is that because of the unbiased nature of a NN model (the overall prediction error is close to zero), the system bias of LDEO TCO₂ could happen to fall between the prediction biases of Gv2 TCO₂ in the surface and interior.

AR: We have now added the bias by area, depth, dataset and method to Table 2.

AC:

	TCO ₂												pCO ₂	
	0-50 m				50-200 m		200-500 m		500-1000 m		>1000 m		0 m	
	LDEO (0 m)		Gv2QC		Gv2QC		Gv2QC		Gv2QC		Gv2QC		LDEO	
	NNGv2LDEO	CANYON-B	NNGv2LDEO	CANYON-B	NNGv2LDEO	CANYON-B	NNGv2LDEO	CANYON-B	NNGv2LDEO	CANYON-B	NNGv2LDEO	CANYON-B	NNGv2LDEO	CANYON-B
Areas defined in Takahashi et al. (2014)														
West GIN Seas	16.8 (7.6)	21.2 (18.1)	14.2 (-1.7)	15.3 (0.7)	6.4 (-0.6)	6.7 (0.3)	5.5 (-1.1)	6.8 (-0.5)	4.1 (0.9)	5 (1.3)	4 (0.8)	4.1 (0.8)	28.6 (17.2)	34.9 (35.2)
East GIN Seas	11.1 (14.1)	9.2 (5.6)	10.2 (1.6)	11.4 (1.3)	5.9 (0.5)	6.2 (2.9)	4.6 (-0.8)	5.2 (1.7)	3.5 (-0.6)	4 (2.3)	3.9 (-0.6)	3.7 (0.1)	17.3 (22.4)	15 (9.4)
High Arctic	13.3 (-8.3)	32.4 (13.7)	20.2 (-1.1)	24.1 (4.4)	11.4 (-0.1)	12.3 (1.7)	6.5 (0.1)	6.6 (-0.2)	6.8 (-0.1)	7.6 (0.6)	6.1 (-0.4)	6.2 (-1.1)	43 (-22.8)	79.1 (22.6)
Beaufort Sea	29.7 (0.8)	42 (10)	54 (0.1)	53.1 (1.3)	14.5 (-1.7)	13.3 (1.8)	8.1 (0.1)	9.2 (-1)	7.5 (2)	8.4 (-0.5)	6.5 (1.1)	7.2 (-2.1)	58.7 (6.7)	135.6 (5.3)
Labrador Sea	5.3 (0.6)	7.5 (2.7)	10.5 (-0.9)	11.6 (1.3)	5.4 (-0.2)	6.6 (1.6)	4.1 (-0.6)	4.3 (1.4)	3.5 (-0.1)	3.7 (1.5)	2.7 (0.2)	3.1 (1.6)	10.7 (1)	13.6 (4.5)
Subarctic Atlantic	11.7 (3.3)	14.6 (11.5)	9 (-2.3)	11.1 (1.5)	4.5 (0.1)	5.4 (1.9)	4.3 (0.1)	4.8 (0.3)	4.2 (0.1)	4.6 (0.4)	4 (-0.2)	4.3 (0)	21.9 (7.8)	26.7 (23.2)
North Atlantic Drift	11.1 (0.5)	12.9 (5.7)	13.3 (-1.3)	14.5 (0.5)	9.9 (0.7)	10.4 (0.5)	7.8 (0)	7.8 (-0.4)	4.3 (0.2)	4.5 (0.1)	3.5 (0.3)	3.6 (-0.1)	21 (1.4)	24.7 (10.3)
Central Atlantic	7.9 (-0.3)	9.6 (-1.2)	15.8 (0)	14.9 (0.3)	6.6 (0.2)	6.5 (1)	5.2 (-0.5)	5.1 (0.5)	4.6 (-0.1)	4.5 (0)	4.3 (0)	4.4 (0)	13.5 (-0.3)	17.4 (-2)
South Atlantic Transition Zone	7.7 (-1.3)	13.8 (-2.1)	7.2 (-0.9)	7.8 (0.3)	5.4 (0.8)	5.7 (0.1)	5.7 (1.1)	4.7 (0.7)	5 (-0.1)	4.8 (1)	4.3 (0.5)	4.2 (0.3)	14.6 (-2.7)	25 (-5.2)
Antarctic Atlantic	11.8 (1.4)	19.2 (20.9)	8.6 (-1.6)	10 (0.5)	4.6 (0)	5.4 (0.4)	3.5 (-0.1)	3.8 (0.3)	3.1 (0.1)	3.1 (0.3)	3.1 (0)	3.1 (0.3)	25.6 (4.9)	41.5 (50.9)
Kuroshio Alaska Gyre	10.9 (1.6)	12.3 (1.5)	8.5 (-0.9)	12.2 (2.4)	6.4 (0.9)	8.1 (0.3)	5 (0.3)	5.2 (1.1)	4.5 (0.6)	4.3 (0.3)	3.7 (0.4)	3.9 (0.3)	20.7 (3.7)	23.7 (3.4)
North Central Pacific	26.3 (-3.6)	34.5 (-9.6)	9.6 (0.2)	15 (3.4)	6.8 (0.5)	8.3 (0.4)	4.2 (0.3)	4.7 (0.5)	4 (-0.3)	4.1 (0.3)	3.4 (0.3)	3.8 (0)	46.7 (-0.4)	56.6 (-7)
Sea of Okhotsk	- -	- -	23.1 (0.9)	16.4 (1.6)	11.3 (-1.2)	6.8 (-0.7)	6.3 (-2.3)	5.1 (-1.6)	5.2 (-4)	3.4 (-1.3)	4.1 (1.2)	3.5 (1.9)	- -	- -
Central Tropical North Pacific	8 (-1.3)	9.7 (-3.2)	7.9 (-0.9)	8.8 (0.5)	7.2 (0.5)	7.2 (1.2)	4.9 (-0.6)	5 (0.2)	4.3 (-0.4)	4.5 (0.5)	3.6 (-0.2)	3.8 (0.2)	14.2 (-2.1)	17.2 (-5.6)

Tropical East North Pacific	11.1	14.5	10.9	13.8	5.9	8.5	2.6	3.4	2.1	2.1	2.4	2.1	20.8	28.2
	(-0.1)	(-4.5)	(0.9)	(-1.4)	(0.3)	(2.5)	(0.3)	(1.7)	(0)	(0.6)	(-0.2)	(-0.3)	(0.2)	(-8.8)
Panama Basin	12.5	17.4	10.2	9.5	6.5	3.9	4	5.8	3.8	3.2	4.2	4.3	25.8	38.8
	(-0.7)	(0.7)	(-3.4)	(1.5)	(-2.7)	(-6.7)	(2.3)	(-1.2)	(0.8)	(1.4)	(0)	(2.8)	(-0.3)	(1.3)
Central South Pacific	10.1	12.9	10.3	10.9	8.9	9.4	4.4	4.5	3.8	3.8	3.3	3.5	18.6	24.3
	(-2.1)	(-3.4)	(1.2)	(-0.7)	(0)	(0.2)	(-0.1)	(0.8)	(-0.1)	(-0.4)	(0)	(-0.1)	(-3)	(-5)
East Central South Pacific	10.7	15.4	10.6	15.2	6.9	7.5	4.1	2.8	3.8	3.5	3.3	3	24.1	34.2
	(-1)	(-0.1)	(0.6)	(1.4)	(1.2)	(1.3)	(0.4)	(0.1)	(-0.5)	(-0.2)	(-0.6)	(0.3)	(-1.2)	(0.5)
Subpolar South Pacific	6.9	7.9	5.8	7.7	5	5.4	2.9	2.8	4.7	4.8	4.1	4.4	13.7	16
	(1.2)	(-0.9)	(-0.7)	(2.4)	(0.4)	(0.6)	(0.9)	(1.7)	(-1)	(1.2)	(0.7)	(1)	(2.4)	(-2.2)
Antarctic Pacific	19.5	29.3	8.3	7	3.6	4.1	2.7	3.3	2.6	2.9	2.6	2.1	34.1	53.8
	(1.9)	(4.9)	(-1.4)	(0.5)	(-0.5)	(0.5)	(-0.1)	(0.7)	(0.3)	(0.3)	(0.5)	(-0.1)	(7.7)	(14.9)
Main North Indian	10.8	13	10.5	12.9	8.1	7.8	3.2	3.3	2.4	2.6	3.1	3.7	19.8	23.5
	(-1.8)	(-7.7)	(2.8)	(1.7)	(-0.1)	(0.5)	(0.7)	(0.9)	(-0.4)	(-0.4)	(-0.2)	(0.2)	(-2.8)	(-12.7)
Red Sea	18.3	20.9	12	16.8	9.4	8.7	7.6	7.9	7.4	5.7	3.3	7.2	28	32.3
	(-13.9)	(-16.7)	(-4.3)	(-3.5)	(0.2)	(-3.7)	(-4.3)	(-5.1)	(1)	(-4.4)	(-1.3)	(-1.1)	(-21)	(-25.5)
Bengal Basin	6	3.7	9.8	7.4	7.4	6.4	2	2.1	1.9	2.1	2	2.2	10.7	6.7
	(1.1)	(-5.5)	(-0.2)	(2)	(0.3)	(1.3)	(0.4)	(1.1)	(0.4)	(-0.2)	(-0.6)	(-0.4)	(1.4)	(-10.2)
Main South Indian	8.1	10.4	9.1	10	7.1	6.9	3.8	3.8	4.2	4.5	3.4	3.8	14	17.7
	(-0.2)	(0.4)	(-0.1)	(1)	(0.3)	(0.6)	(-0.1)	(0.9)	(0.1)	(1.1)	(0.1)	(0.1)	(-0.1)	(0.9)
South Indian Transition	8	9.4	5.3	5.3	4.1	4.4	4	3.7	3.9	3.4	3.4	3.7	16	18.8
	(-0.4)	(0.7)	(-1.7)	(-0.4)	(0.8)	(0.8)	(0)	(0.5)	(-0.2)	(0.3)	(-0.6)	(-0.9)	(-0.7)	(1.9)
Antarctic Indian	9.7	11.8	6	6.8	4.1	4.7	3	3.3	2.5	2.6	2.7	2.6	23.2	28.7
	(1.1)	(5.9)	(-1.4)	(0.2)	(0.4)	(0.6)	(0.1)	(0.3)	(-0.3)	(0.3)	(0.3)	(0.5)	(3.9)	(15.3)
Cicum polar Southern Ocean	15.9	24.5	7.6	8.2	4.4	4.9	3.1	3.4	2.9	2.9	2.9	2.7	30.7	48.9
	(0.9)	(9.8)	(-1.6)	(0.4)	(-0.2)	(0.3)	(-0.1)	(0.2)	(0)	(0.2)	(0.1)	(0.2)	(4.7)	(25.7)
Weighted	11.1	15	11	12.1	6.6	7	4.3	4.5	4	4.1	3.5	3.7	21.1	29.6
	(0)	(2.8)	(-0.5)	(0.8)	(0.2)	(0.8)	(-0.1)	(0.5)	(-0.1)	(0.3)	(0.1)	(0.2)	(1.3)	(7.5)

RC: Absolute errors are often used in tables and figures. They hide the information whether the errors show under-estimate or over-estimate; Therefore, showing negative errors are recommended.

AR: We have added the bias in all the tables where RMSE is computed. The figures where absolute differences were shown have been changed for the equivalent with the differences to show negative errors.

RC: Line 132: The reference of Rumelhart et al. (1986) is missing.

AR: Thanks. Added.

RC: Line 149-152: Could you give more details on how to ensure biogeochemical variables have a larger influence than position variables?

AR: We have added more information about the method to extract the influence of each input variable in the computed TCO₂.

AC: In Section 2.1: “The influence of each input variable on the computed TCO₂ was obtained from Eq. (1):

$$C_i = \sum_{k=1}^H w_{ik} \cdot w_k$$

where C_i is the relative importance of the input variable i , H the number of neurons in the hidden layer, w_{ik} the weight of the connection between the variable i and the neuron k of the hidden layer and w_k is the weight of the connection between the neuron k of the hidden layer and output layer.”

In Section 3.1: “For this network, the influence of each input variable on the computed TCO₂ is depicted in Fig. S2. The position variables together (latitude, longitude, slongitude and depth) have no more than 30% influence, allowing biogeochemical variables to be the main ones responsible for the variability of TCO₂. Furthermore, the input variable year has an influence lower than 5%. This is probably responsible for capturing the positive interannual trend due to the TCO₂ increase derived from anthropogenic emissions of CO₂ to the atmosphere (see Sect. 3.2).”

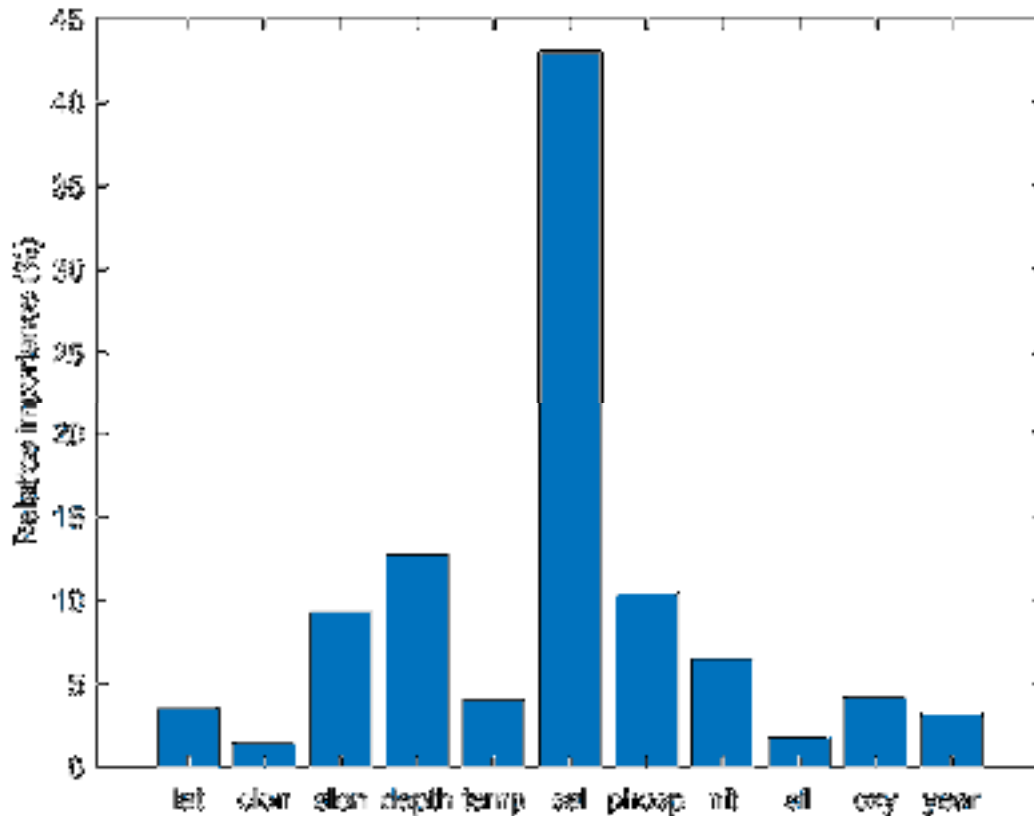


Figure S2. The relative importance of the input variables for NNGv2LDEO. lat: latitude; lon: longitude; slon: slongitude; temp: temperature; sal: salinity; phosp: phosphate; nit: nitrate; sil: silicate; oxy: oxygen.

RC: Line 254: Why average 1981 to 2015 to obtain 1995 climatology? You have 20 year from 1995 to 2015, but only 14 year from 1981 to 2015.

AR: We averaged 1981 to 2010 because the mean year is 1995. We wrote the wrong year "2015" in the previous manuscript. Therefore, the period has 30 years.

RC: Line 261: This is an important criterion to select the NN for making prediction, but no detail available. Could you supply more information in the supplement material on the influences of position variable of the networks?

AR: Position is essentially added to try to capture processes that change TCO_2 that are not reflected through the biogeochemical variables used in this study. For example, the mentioned A_T and TCO_2 carried by rivers to the ocean, that modify the typical relations with other variables, like salinity- A_T . We have given more information about the influence of the position variable, which was shown in a previous comment.

RC: Table 2. Are the errors absolute? If so, please state explicitly. Also, the global errors should be added. Showing negative errors are more meaningful.

AR: We have added the bias to Table 2 to show negative errors.

RC: Table 6: Does the label “NNGv2” means NNGv2LDEO?

AR: It was a mistake. It should be NNGv2LDEO. Thanks. Changed.

RC: Table 7: Is the bias absolute? If so, please state explicitly. The global errors should be added. Showing negative errors are more meaningful.

AR: Biases were always obtained through the manuscript as the difference between the measured (or computed by other methods) TCO₂ and the one computed by the neural network. We have added a clarification in the methods section.

AC: “It should be noted that the RMSE and the bias were obtained for all the comparisons, the last statistic being computed as the difference between the measured (or computed by the method to compare) TCO₂ and the one obtained with the neural network of the present study.”

RC: Figure 1b: “ $y=1x +- 7.8$ ” should be $y=1x - 7.8$.

AR: Thanks. Changed.

RC: Figure 3: Showing negative errors are more meaningful.

AR: Changed.

AC:

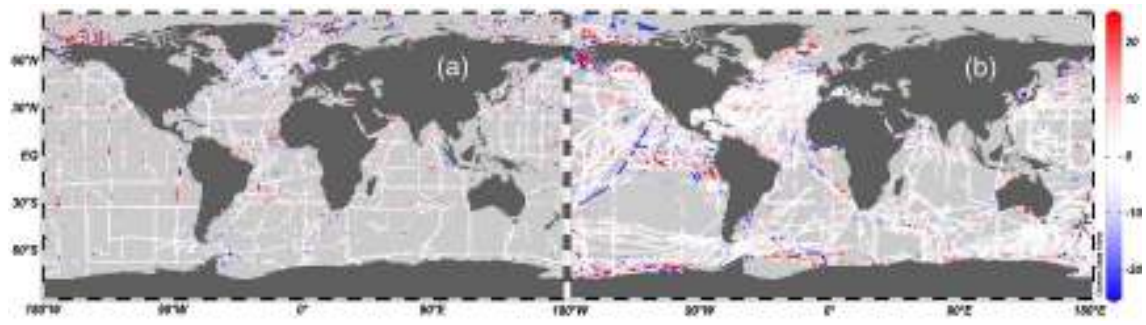


Figure 3. Differences between (a) Gv2 TCO2 and NNGv2LDEO TCO2 (0-30 m) and (b) LDEO TCO2 and NNGv2LDEO TCO2 (0 m).

RC: Figure 4b: The error bar for depth < 50m should be added using the surface errors.

AR: Added.

AC:

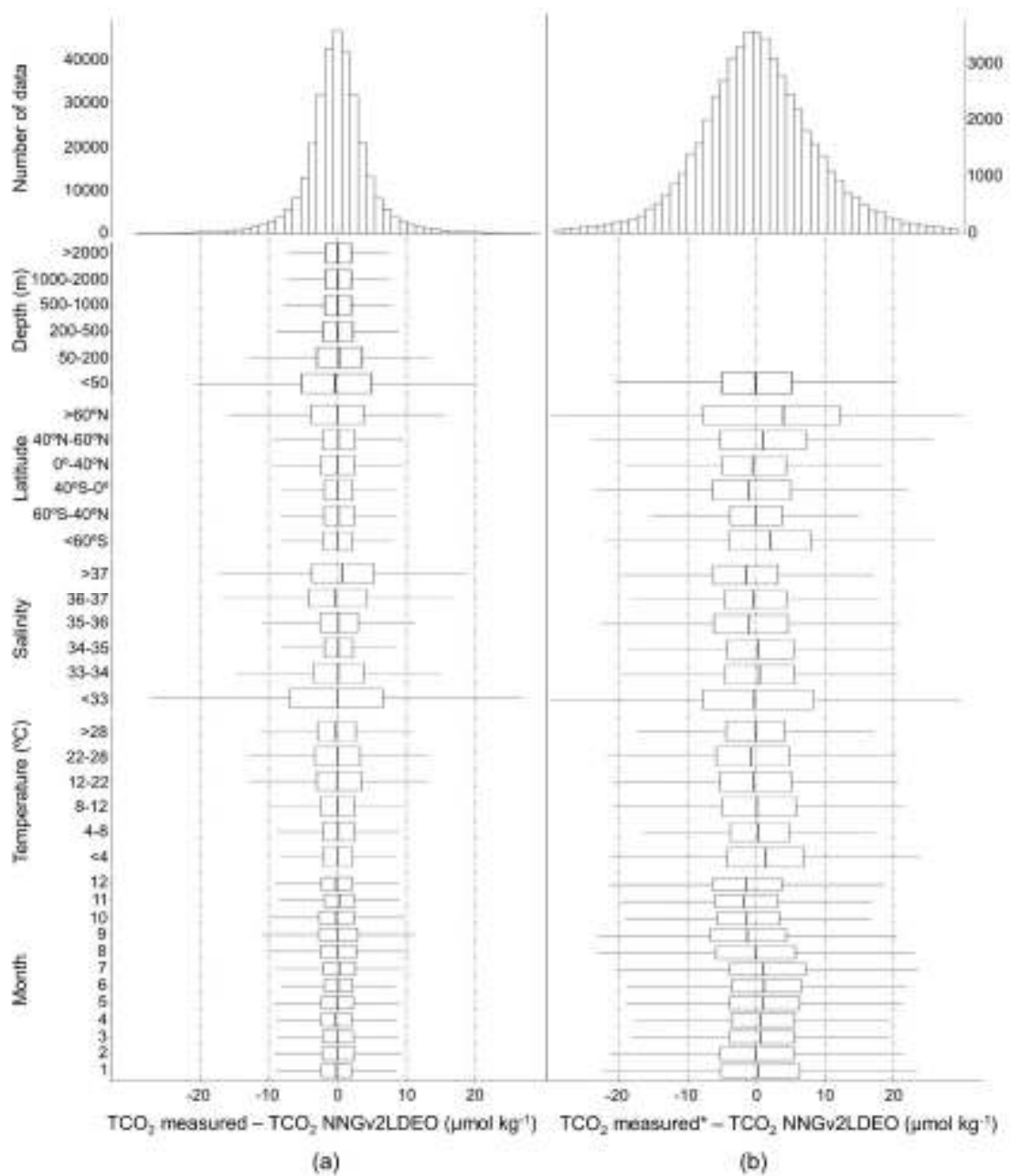


Figure 4. Histograms and box plots of differences between measured and neural network computed TCO₂ in (a) Gv2 and (b) LDEO. *TCO₂ computed from measured pCO₂ and neural network derived A_T.

RC: Figure S1.b: There should be a “+” operator between $b_j * a_0$ and $\text{SUM}(w_{ij} * a_i)$ in the activation function.

AR: Thanks. Changed.

AC:

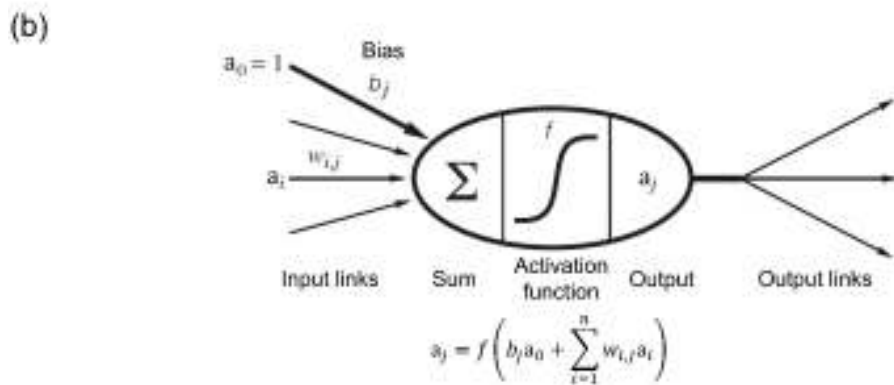
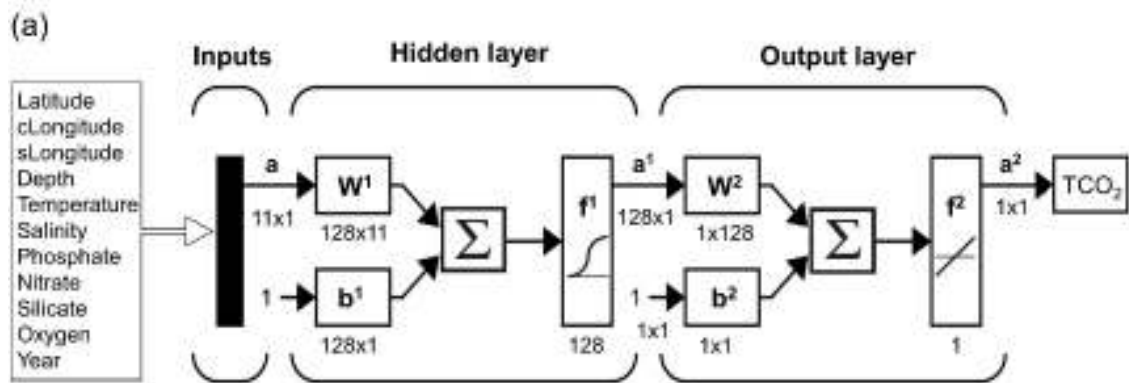


Figure S1. (a) Neural network configuration. The notation is in agreement with Hagan et al. (2014). \mathbf{a} : input vectors; \mathbf{W} : weight matrix; \mathbf{b} : bias matrix; Σ : sum; f : transfer function; \mathbf{a}^x : output matrix. The superscripts indicate the number of the layer. $cLongitude = \cos(\frac{\pi}{180^\circ} longitude)$; $sLongitude = \sin(\frac{\pi}{180^\circ} longitude)$. The dimensions of the matrices are for an individual sample. Modified from Hagan et al. (2014). (b) Neuron. a_i : inputs to each neuron; $w_{i,j}$: weights of each input to each neuron. Modified from Russell and Norvig et al. (2010).

RC: Figure S2: How the std is calculated for T, S, and pCO₂. Modelled TCO₂ is larger than observed TCO₂ for all pCO₂ STD > 4. How to explain this?

AR: In Fig. S2 the boxplot is obtained by ranges of std of the three mentioned variables: T, S and pCO₂. These std were obtained from the monthly average carried out in each 1°x1° pixel from the LDEO data, as is explained in L.160-L.164: “The pCO₂, temperature and salinity data from LDEO were monthly-averaged for each year in a 1°x1° grid. The points where the standard deviation (std) of the averaged pCO₂, temperature and salinity were greater than ±20 μatm, 1.5°C and 0.5, respectively, were discarded, since the objective is to capture the monthly variability and therefore an extremely high sub-monthly variability could lead to errors.”

The measured TCO₂ is the larger one, since the boxplot has been obtained with the difference: measured TCO₂ minus NN computed TCO₂ (as is depicted in the x axis label). With the increase of the std of pCO₂, the error increases because of the difficulty to model the high sub-monthly variability of pCO₂, which is not the purpose of this study, obtaining a bias of ~2 μatm for pCO₂ std > 12.

We have changed the captions in Fig. S2 (now Fig. S3) to clarify how std was calculated.

AC:

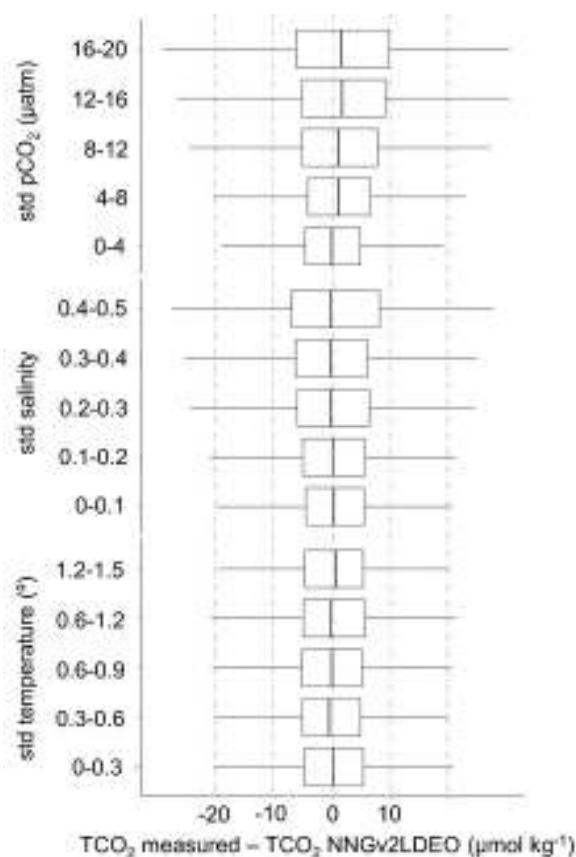


Figure S3. Box plots of differences between measured and computed TCO₂ in LDEO by standard deviation (std) ranges obtained from the monthly average of the LDEO data.

RC: Figure S3. If the difference is absolute, please state clearly. Showing negative errors are more meaningful.

AR: We have changed Fig. S3 (now Fig. S4) to show negative errors too.

AC:

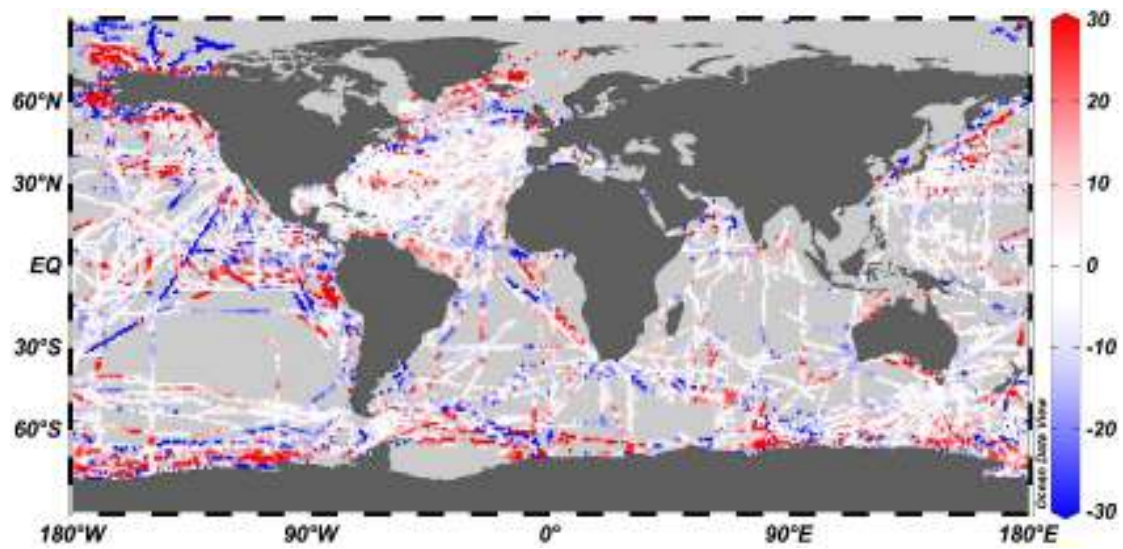


Figure S4. Differences between measured and computed pCO₂ with AT from NNGv2 (Broullón et al., 2019) and TCO₂ from NNGv2LDEO in LDEO. Units are microatmospheres (µatm).

RC: Figure S5 and S6: Showing negative errors are more meaningful.

AR: Changed.

AC:

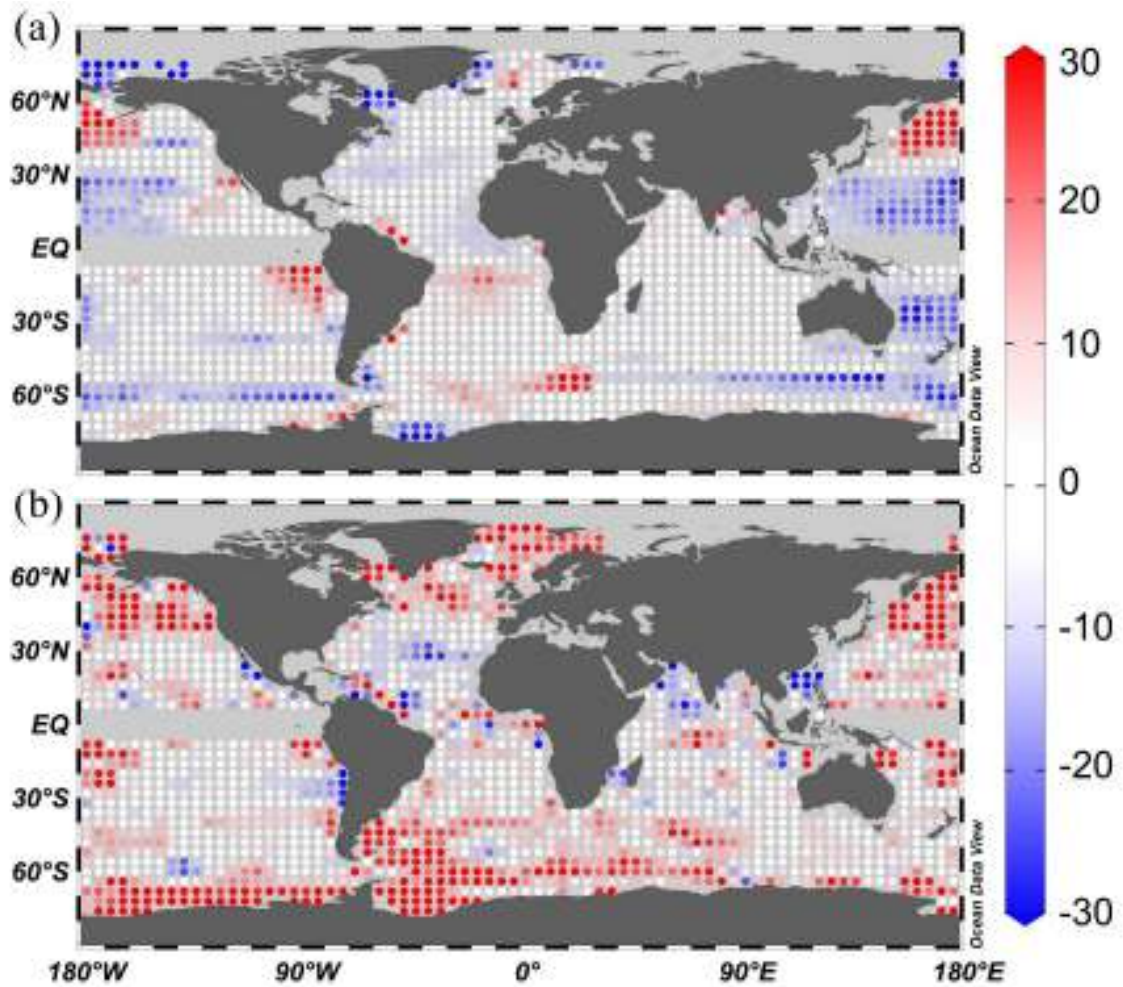


Figure S6. Differences between the annual mean of the surface TCO₂ neural network climatology and (a) Takahashi et al. (2014) and (b) Lauvset et al. (2016) surface annual mean climatology. Units are micromole per kilogram ($\mu\text{mol kg}^{-1}$). The color bar was developed in order to show the highest differences beyond the errors of each method. This figure was made with Ocean Data View (Schlitzer, 2016).

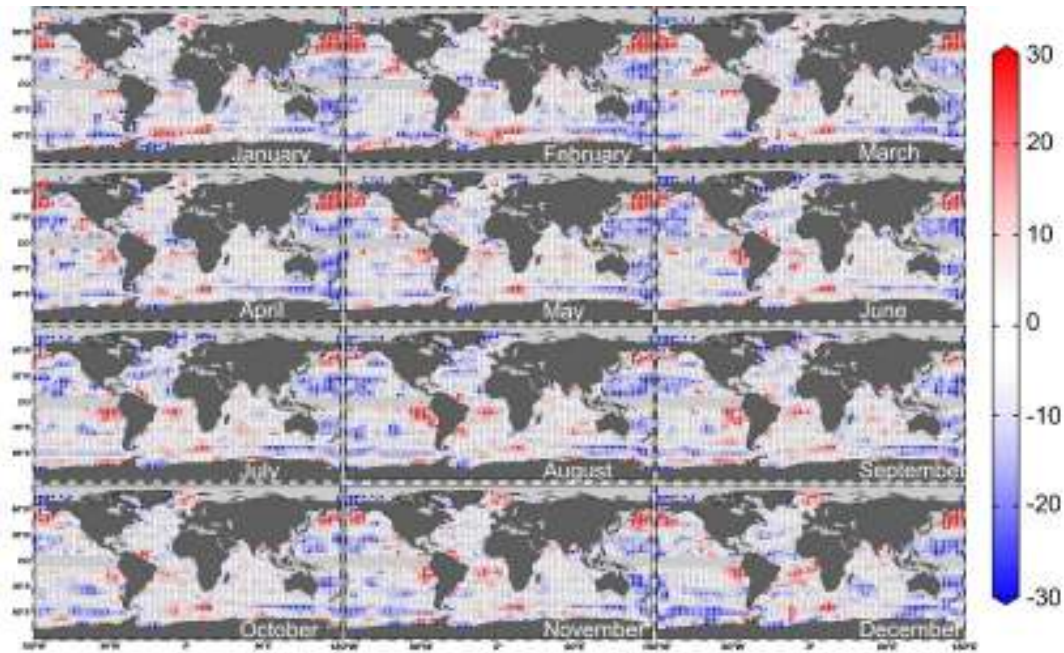


Figure S7. Differences between the monthly climatology of TCO₂ of Takahashi et al. (2014) and the one of the present study. The color bar was developed in order to show the highest differences beyond the errors of each method. Units are micromole per kilogram ($\mu\text{mol kg}^{-1}$). This figure was made with Ocean Data View (Schlitzer, 2016).

RC: Figure S7a: The model produces a much larger seasonal amplitude in the surface water. Unless measurements are not available in all months, the seasonal amplitude of the climatology should be no larger than that of the measurements. Does this indicate either over-fitting or extrapolation in seasons of no measurements.

AR: There are no measured values larger than the red limits in BATS (Fig. S7(a); now Fig. S8(a)), but there are in Gv2LDEO dataset, with which the network was trained. Therefore, the larger amplitude is not because overfitting nor extrapolation. Furthermore, the differences are inside the error of the network in the surface layer (Table 2, Central Atlantic: $7.9 \mu\text{mol/kg}$ (LDEO) and $15.8 \mu\text{mol/kg}$ (Gv2 in the 0-50 m layer)).

RC: Figure S8 and S9. Plotting land with colors confuses grasping the contours of differences.

AR: Changed.

AC:

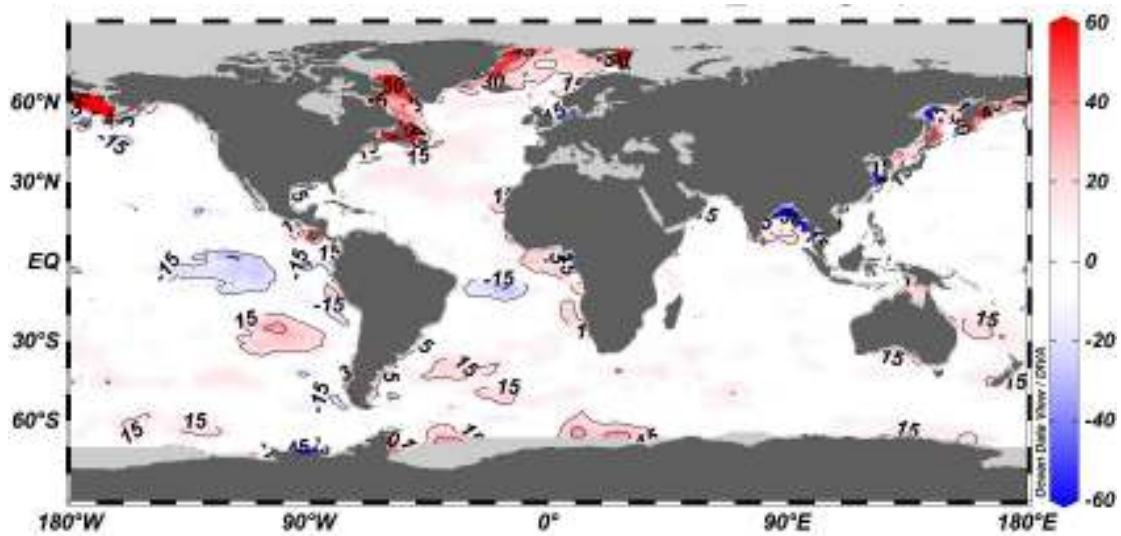


Figure S10. Differences between the annual mean climatology of pCO₂ from Landschützer et al. (2017) centered in 1995 and the one computed in the present study. Units are microatmospheres (µatm). The contour lines of 15, 30, 45 and 60 µatm are shown. This figure was made with Ocean Data View (Schlitzer, 2016).

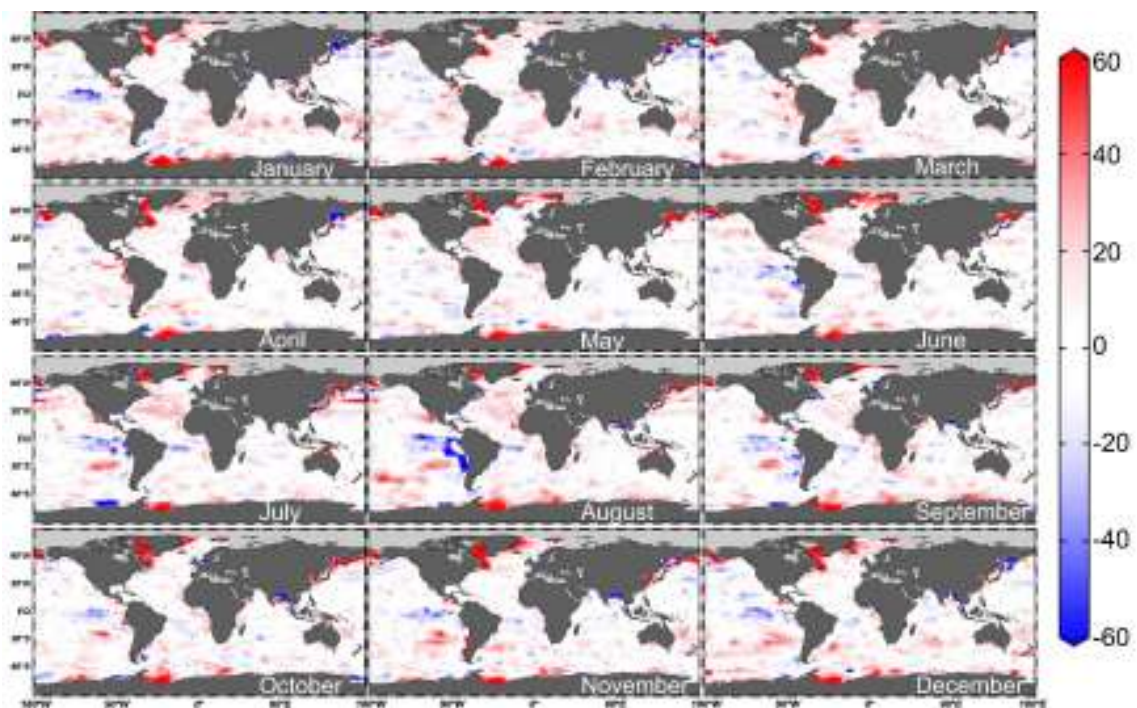


Figure S11. Differences between the monthly climatology of pCO₂ from Landschützer et al. (2017) centered in 1995 and the one computed in the present study. Units are microatmospheres (µatm). This figure was made with Ocean Data View (Schlitzer, 2016).

A global monthly climatology of oceanic total dissolved inorganic carbon: a neural network approach

Daniel Broullón¹, Fiz F. Pérez¹, Antón Velo¹, Mario Hoppema², Are Olsen³, Taro Takahashi^{4,†}, Robert M. Key⁵, Toste Tanhua⁶, J. Magdalena Santana-Casiano⁷ and Alex Kozyr⁸

¹Instituto de Investigaciones Marinas, CSIC, Eduardo Cabello 6, 36208 Vigo, Spain

²Alfred Wegener Institute Helmholtz Centre for Polar and Marine Research, Postfach 120161, 27515 Bremerhaven, Germany

³Geophysical Institute, University of Bergen and Bjerknes Centre for Climate Research, Allégaten 70, 5007 Bergen, Norway

⁴Lamont-Doherty Earth Observatory of Columbia University, Palisades, NY 10964, USA

⁵Atmospheric and Oceanic Sciences, Princeton University, 300 Forrester Road, Sayre Hall, Princeton, NJ 08544, USA

⁶GEOMAR Helmholtz Centre for Ocean Research Kiel, Düsternbrooker Weg 20D-24105 Kiel, Germany

⁷Instituto de Oceanografía y Cambio Global, IOCAG, Universidad de Las Palmas de Gran Canaria, Las Palmas de Gran Canaria, Spain

⁸NOAA National Centers for Environmental Information, 1315 East-West Hwy Silver Spring, MD 20910 USA

[†]Deceased

Correspondence to: Daniel Broullón (dbroullon@iim.csic.es)

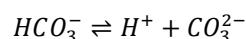
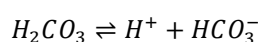
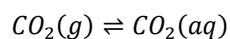
Abstract

Anthropogenic emissions of CO₂ to the atmosphere have modified the carbon cycle for more than two centuries. As the ocean stores most of the carbon on our planet, there is an important task in unraveling the natural and anthropogenic processes that drive the carbon cycle at different spatial and temporal scales. We contribute to this by designing a global monthly climatology of total dissolved inorganic carbon (TCO₂) which offers a robust basis in carbon cycle modeling but also for other studies related to this cycle. A feedforward neural network (dubbed NNGv2LDEO) was configured to extract from the Global Ocean Data Analysis Project version 2.2019 (GLODAPv2.2019) and the Lamont-Doherty Earth Observatory (LDEO) datasets the relations between TCO₂ and a set of variables related to the former's variability. The global root-mean-squared error (RMSE) of mapping TCO₂ is relatively low for the two datasets (GLODAPv2.2019: 7.2 μmol kg⁻¹; LDEO: 11.4 μmol kg⁻¹) and also for independent data, suggesting that the network does not overfit possible errors in data. The ability of NNGv2LDEO in capturing the monthly

variability of TCO₂ was testified through the good reproduction of the seasonal cycle in ten time-series
35 stations spread over different regions of the ocean (RMSE: 3.6 to 13.1 μmol kg⁻¹). The climatology was
obtained by passing through NNGv2LDEO the monthly climatological fields of temperature, salinity and
oxygen from World Ocean Atlas 2013, and phosphate, nitrate and silicate computed from a neural network
fed with the previous fields. The resolution is 1° x 1° in the horizontal, 102 depth levels (0-5500m) and
40 monthly (0-1500 m) to annual (1550-5500 m), and it is centered in the year 1995. The uncertainty of the
climatology is low when compared with climatological values derived from measured TCO₂ in the largest
time-series stations. Furthermore, a computed climatology of partial pressure of CO₂ (pCO₂) from a
previous climatology of total alkalinity and the present one of TCO₂ supports the robustness of this product
through the good correlation with a widely used pCO₂ climatology (Landschützer et al., 2017). Our TCO₂
climatology is distributed through the data repository of the Spanish National Research Council (CSIC;
45 <http://dx.doi.org/10.20350/digitalCSIC/10551>, Broullón et al., 2020).

1 Introduction

The ocean is the major carbon reservoir of the Earth. Most of this carbon occurs as dissolved inorganic
carbon (TCO₂, also known as DIC or C_T) (Ciais et al., 2013; Tanhua et al., 2013). Three species make up
TCO₂: dissolved CO₂ (generally considered as the sum of the dissolved CO₂ itself (CO₂(aq)) and carbonic
50 acid (H₂CO₃)), bicarbonate ion (HCO₃⁻) and carbonate ion (CO₃²⁻). The relative concentrations of these
species with respect to each other determine the seawater pH (Zeebe and Wolf-Gladrow, 2001). The
seawater CO₂ chemistry system can be represented as a set of chemical equilibria reactions that describes
the speciation of the various ions of TCO₂ as follows:



Since the Industrial Revolution, the concentration of TCO₂ in the global ocean has increased, generally to
a certain depth level (depending on the particular processes in each ocean area) due to the entry of CO₂ into
60 the seawater from the atmosphere (Sarmiento and Gruber, 2002; Doney et al., 2009; Vázquez-Rodríguez et
al., 2009; Bates et al., 2012; Sallée et al., 2012; Khatiwala et al., 2013). The uptake is driven by the
increasing partial pressure of CO₂ (pCO₂) in the atmosphere relative to the ocean, generated by the
anthropogenic emissions of CO₂ that cause an annual net flux of this gas into the ocean (Le Quéré et al.,
2018). Accompanying the change in TCO₂, the pH and carbonate ion concentration have been declining
65 because of the anthropogenic process previously mentioned, these changes being reflected in the
proportions of the chemical species of TCO₂ (Kleypas and Langdon, 2000; Orr et al., 2005). These changes
in seawater chemistry framed in the ocean acidification process can negatively influence various processes

involving marine organisms such as calcification, growth and survival (Orr et al., 2005; Fabry et al., 2008; Hendriks et al., 2010; Hoegh-Guldberg and Bruno, 2010; Kroeker et al., 2013).

70 In addition to the secular trends driven by the uptake of anthropogenic CO₂, ocean TCO₂ varies both temporally and spatially as a consequence of several natural processes. This variability may reach values of 15% of the mean TCO₂ value in the ocean (Lee et al., 2000). The processes that increase TCO₂ are: net flux of CO₂ from the atmosphere to the ocean, organic matter remineralization and the dissolution of calcium carbonate (CaCO₃). The processes that reduce TCO₂ are: net flux of CO₂ from the ocean to the
75 atmosphere, primary production and calcification. Advection and mixing also influence the variability of TCO₂ in these two ways (Sabine et al., 2002). In the surface ocean, the main variables influencing the variability of TCO₂ are temperature and salinity (Weiss et al., 1982; Lee et al., 2000; Wu et al., 2019) through the modification of the solubility of CO₂, affecting the seawater pCO₂ (which is almost instantaneous) and thus the air-sea CO₂ flux, which eventually drives the change in TCO₂ over time..
80 Nutrients and oxygen can also reflect the processes that modify the concentration of TCO₂ through their consumption and release, like during the cycling of organic matter (Körtzinger et al., 2001; Bauer et al., 2013). From products generated with measured data (Key et al., 2004; Takahashi et al., 2014; Lauvset et al., 2016) and in modeling studies (e.g., Doi et al., 2015), it is known that the global surface distribution of TCO₂ follows a zonal gradient: there is a reduction of its concentration from the poles to the equator
85 reflecting the processes that control its variability. Key et al. (2004) emphasize that this distribution is associated to the distribution pattern of nutrients. Recently, Wu et al. (2019) found that the distribution of surface salinity-normalized TCO₂ (nDIC) has two main drivers: temperature and upwelling. At depth, the variation shown in almost any measured profile of TCO₂ mainly reflects the remineralization of organic matter and, to a lesser extent, the dissolution of CaCO₃ (Millero, 2007), resulting in an increase in TCO₂
90 from the surface to the intermediate depths.

Understanding the distribution and variability of TCO₂ in the ocean and its secular trends driven by anthropogenic carbon uptake is needed to assess the magnitude and possible impacts of ocean acidification. It is also necessary for the evaluation of numerical models that include the carbon cycle and their estimates of past, current and future ocean carbon cycle behavior (e.g., Yool et al., 2013; Aumont et al., 2015;
95 Butenschön et al., 2016; Le Quéré et al., 2016; Goris et al., 2018). Seasonality of TCO₂ and the horizontal and vertical variability underscore the necessity to design a climatology with both monthly and spatial resolutions according to the processes that influence this variable on a global scale. The existing climatologies of TCO₂ do not include all these characteristics collected together. Key et al. (2004) and Lauvset et al. (2016) built an annual climatology in 33 depth levels using interpolation techniques over data
100 from Global Ocean Data Analysis Project version 1 (GLODAPv1; Key et al., 2004) and GLODAPv2 (Key et al., 2015; Olsen et al., 2016), respectively. Takahashi et al. (2014) published a monthly climatology for the surface ocean computed from climatologies of pCO₂ and total alkalinity (A_T). Other studies used the co-variability between TCO₂ and other more commonly measured variables discussed above for mapping/gap-filling via empirical regressions and neural networks. Lee et al. (2000) used temperature and
105 nitrate to compute surface nDIC with an area-weighted error of ±7 μmol kg⁻¹. Sauzède et al. (2017) and Bittig et al. (2018) trained neural networks with GLODAPv2 data to compute TCO₂ over the depth range

0-8000 m with an accuracy of $\pm 9 \mu\text{mol kg}^{-1}$ and $\pm 7.1 \mu\text{mol kg}^{-1}$, respectively. The input variables used in those studies were location, pressure, temperature, salinity, dissolved oxygen and time.

110 In the present study, we introduce the use of neural networks for going one step further in the design of a climatology. We have generated a climatology of TCO_2 with a resolution consistent with that of the climatology of A_T of Broullón et al. (2019): horizontal resolution of $1^\circ \times 1^\circ$, 102 depth levels between 0 and 5500 m and a monthly (0-1500 m) and annual (1550-5500 m) temporal resolution. The availability of global databases containing variables of the seawater CO_2 system with more and more data (e.g., GLODAPv2.2019, Lamont-Doherty Earth Observatory database (LDEO; Takahashi et al., 2017), Surface
115 Ocean CO_2 Atlas (SOCAT; Bakker et al., 2016)) and the great ability of the neural networks to interpolate as shown in other climatological studies about CO_2 system variables (Landschützer et al., 2014; Broullón et al., 2019), show the appropriateness of this approach for generating a global monthly climatology covering more than the surface ocean.

2 Methodology

120 2.1 Neural network design

A feed-forward neural network was configured to compute TCO_2 in the global ocean and to create a global climatology based on the good results previously obtained with this method in similar studies (e.g., Broullón et al., 2019). Briefly, a neural network of this type (Fig. S1a) is used to extract relationships between a set of input variables and a target one through a training process. At this stage, the inputs are passed through
125 different parallel layers composed by a tunable number of neurons to reach values as closest as possible to the target ones (Fig. S1a). Initially, all inputs enter in each neuron of the first layer where they are being multiplied by different weights depending on the neuron they go. Inside the neurons (Fig. S1b), the results of the previous operation are summed and a bias is added. The obtained value inside each neuron is passed through an activation function which yields an output. The outputs of each neuron in each layer go to the
130 following layer suffering the same process described to this point. In the last layer, which is composed by one neuron, a unique value for the target variable is calculated for each pair of inputs-target. This value is compared to the desired one and the difference between both values is backpropagated through the entire network in order to adjust the weights and biases, and to start again the processes and reach an accurate output value after multiple iterations. A complete description of the most common algorithms used to
135 backpropagate and minimize the errors can be founded in Rumelhart et al. (1986), Levenberg (1944) and Marquardt (1963).

The method used here is equivalent to that fully described by Broullón et al. (2019) for A_T . In addition to the target variable (TCO_2 instead of A_T), the main changes in the present study compared to that of Broullón et al (2019) are the inclusion of the input variable “year”, accounting for the anthropogenic increase of the
140 TCO_2 pool, and the use of the pCO_2 database from LDEO (Takahashi et al., 2017) in addition to the extended GLODAPv2.2019 (Olsen et al. 2019) to enable more robust TCO_2 estimates in the surface ocean. Similar to Broullón et al. (2019), the neural networks were trained using the Levenberg-Marquardt method (Levenberg, 1944; Marquardt, 1963) through the *trainlm* function (detailed in Beale et al., 2018) in

MATLAB. The splitting of the database used in the present study (see Sect. 2.2) in the sets needed for
 145 training and testing the network is depicted in Fig. 1. The data were randomly associated to each dataset to
 capture (training) and evaluate (test) all possible variability. The input variables are temperature, salinity,
 phosphate, nitrate, silicate, oxygen, sample position and year (Fig. S1a). The number of neurons tested in
 the unique hidden layer to find the best neural network was 16, 32, 64, 128 and 256. Ten networks were
 150 trained for each number of neurons. The criteria to select the final number of neurons are based on a trade-
 off between the root-mean-squared error (RMSE — between the measured TCO₂ and that estimated by the
 neural network) on the one hand, and the generalization of the network (to prevent overfitting, maintaining
 a similar error in the training and in the test sets) on the other hand. Furthermore, an additional criterion
 based on the influence of each input variable on the TCO₂ extracted with the connection weight approach
 (Olden and Jackson, 2002) was followed to ensure that biogeochemical input variables have a larger
 155 influence on the TCO₂ estimates than the input variables related to sample position for selecting a proper
 network. The influence of each input variable on the computed TCO₂ was obtained from Eq. (1):

$$C_i = \sum_{k=1}^H w_{ik} \cdot w_k \quad (1)$$

where C_i is the relative importance of the input variable i , H the number of neurons in the hidden layer,
 w_{ik} the weight of the connection between the variable i and the neuron k of the hidden layer, and w_k is the
 160 weight of the connection between the neuron k of the hidden layer and output layer.

2.2 Data

We included the LDEO database version 2016 (Takahashi et al., 2017;
https://www.nodc.noaa.gov/ocads/oceans/LDEO_Underway_Database, last access: 13 November 2017),
 because it contains significantly more data in the surface layer than GLODAPv2.2019. Since the higher
 165 variability in the surface layer may lead to high errors in modeling variables of the seawater CO₂ system
 (e.g., Carter et al., 2018; Bittig et al., 2018; Broullón et al., 2019), including the LDEO database should
 force the network to reach a more robust fit. The idea is that these additional data probably have more
 different relationships between input variables and TCO₂ to help the neural network to adequately capture
 spatiotemporal variability. The pCO₂, temperature and salinity data from LDEO were monthly-averaged
 170 for each year in a 1°x1° grid. The points where the standard deviation of the averaged pCO₂, temperature
 and salinity were greater than ±20 µatm, 1.5°C and 0.5, respectively, were discarded, since the objective is
 to capture the monthly variability and therefore an extremely high sub-monthly variability could lead to
 errors. To obtain TCO₂ values from the LDEO data, an additional variable of the CO₂ system is necessary,
 for which we take A_T computed using the neural network NNGv2 of Broullón et al. (2019). The input
 175 variables required by NNGv2 were obtained from: 1) temperature and salinity from LDEO; 2) filtered
 oxygen from World Ocean Atlas version 2013 (WOA13; see Broullón et al., 2019); 3) phosphate, nitrate
 and silicate computed with CANYON-B (Bittig et al., 2018) using the previous variables as inputs. Finally,
 TCO₂ was calculated from this A_T and the averaged pCO₂ using the MATLAB-version of the CO₂SYS
 program (van Heuven et al., 2011); we used the dissociation constants of Mehrbach et al. (1973) (as refit
 180 by Dickson and Millero, 1987) and the borate dissociation constant of Dickson (1990). Note that we used

this software and set of constants for all seawater CO₂ chemistry calculations in the present study. The thus calculated TCO₂ and the associated input variables were used as a part of the training and testing data for the neural networks created here. The final number of data points derived from LDEO was 54572.

185 To represent interior ocean conditions, the GLODAPv2.2019 database (Olsen et al., 2019) was added to the LDEO dataset for training and testing the neural network. Only samples which had data for all input variables and TCO₂ were used. This database was included in two ways: 1) Only samples where all variables passed the 2nd quality control (n=287953) (Olsen et al., 2016; Olsen et al., 2019; hereafter abbreviated Gv2QC) and 2) all samples (n=321647) (hereafter abbreviated Gv2). Therefore, two neural networks options were trained and tested: NNGv2QCLDEO and NNGv2LDEO, respectively.

190 **2.3 Comparison of methods**

We compared our method with CANYON-B of Bittig et al. (2018), where also TCO₂ values were computed from multiple input variables. Both methods are based on neural networks but with certain differences as summarized in Table 1.

195 An error analysis was carried out in the same areas for which this was done by Broullón et al. (2019) for A_T and in several depth ranges (0-50 m, 50-200 m, 200-500 m, 500-1000 m and 1000 m-bottom) for the two methods (our method and CANYON-B) and for the two datasets (Gv2QC and LDEO). The Gv2QC database was analyzed in this section instead of Gv2 because in the designing of CANYON-B only quality-controlled data were included. The analysis of CANYON-B using the LDEO dataset is useful to evaluate the validity of the approach followed by converting pCO₂ to TCO₂ since CANYON-B has not been trained
200 with this dataset.

Computed pCO₂ from A_T and TCO₂ derived from neural networks was also evaluated in the LDEO dataset to assess the adequacy of including this dataset in our approach and to assess the ability of NNGv2 of Broullón et al. (2019) and the present TCO₂ neural network to compute other variables of the seawater CO₂ system. Furthermore, we compared the magnitude of the errors with the ones obtained by Landschützer et al. (2014), in which pCO₂ is computed directly with a neural network, to evaluate the accuracy of our
205 computed pCO₂.

2.4 Validation

In addition to the ability of computing TCO₂ using the Gv2 and LDEO test sets, the neural network has been tested using independent data from ten ocean time series, located in different regions of the world
210 ocean (data were obtained from https://www.nodc.noaa.gov/ocads/oceans/time_series_moorings.html, last access: 4 June 2019): Hawaii Ocean Time-series (HOT ALOHA and HOT ALOHA SURFACE; Dore et al., 2009), Bermuda Atlantic Time-series Study (BATS; Bates et al., 2012), European Station for Time-series in the Ocean at the Canary Islands (ESTOC; González-Dávila et al., 2010), Iceland Sea Time-series (ICELAND; Olafsson et al., 2010) Irminger Sea Time-series (IRMINGER; Olafsson et al., 2010), Kyodo
215 North Pacific Ocean Time-series (KNOT; Wakita et al., 2010), K2 (Wakita et al., 2010), Ocean Weather Station Mike (OWS; Gislefoss et al., 1998) and Kerguelen Islands in the Indian sector of the Southern

Ocean (KERFIX; Jeandel et al., 1998). CANYON-B was also used to compute TCO_2 in the time series to show the differences between that method and ours. The TCO_2 values were obtained by feeding the neural networks with the measured values of the input variables at each time series. The data from these time series allow us to test the ability of the neural network to reconstruct not only the seasonal variability of TCO_2 at the various locations and depths sampled, but also its long-term trends. For the trend analyses, the measured and estimated TCO_2 values were deseasonalized following Bates et al. (2014).

As an additional test, the measured pCO_2 or the pCO_2 calculated from measured TCO_2 and A_T at the time series stations were compared with pCO_2 calculated from the neural network generated values of A_T and TCO_2 . This provides insight in the combined performance of the NNGv2 of Broullón et al. (2019) and the neural network designed in the present study. Furthermore, we compared the magnitude of the errors to that obtained by Landschützer et al. (2014) for some of the time series.

2.5 Climatology of TCO_2

We used the selected network, based on the results of the analyses described above, to construct a climatology of TCO_2 . Climatologies of the input variables were passed through the network to obtain the climatological fields of TCO_2 . The spatiotemporal resolution of the product is determined by that of the climatologies used as inputs: $1^\circ \times 1^\circ$ horizontal resolution, 102 upper depth levels of the WOA13 and monthly (for 0-1500 m depth) to annual (for 1550-5500 m depth) temporal resolution. Temperature and salinity climatologies were obtained from WOA13 objectively analyzed fields (Locarnini et al., 2013; Zweng et al., 2013; <https://www.nodc.noaa.gov/OC5/woa13/woa13data.html>, last access: 6 February 2017). Oxygen, phosphate, nitrate and silicate climatologies were taken from Broullón et al. (2019) (<http://dx.doi.org/10.20350/digitalCSIC/8644>, last access: 1 August 2019). These climatologies of nutrients were created using the objectively analyzed climatologies of temperature, salinity and oxygen (Garcia et al., 2014 filtered, see Broullón et al. (2019)) from WOA13 in CANYON-B (Bittig et al., 2018). As a year input is needed, we decided to center the TCO_2 climatology in 1995 based on the time distribution of the data used to create the WOA13 climatologies: World Ocean Database 2013 (Boyer et al., 2013).

The computed climatological values were compared with those from measured data to assess the uncertainty of the climatology, since WOA13 does not offer an uncertainty field with the objectively analyzed climatologies. Unfortunately, only two locations have enough measured data to calculate a pure climatological value of TCO_2 for each month: HOT ALOHA and BATS. The measured values were monthly averaged at several depth levels and the anthropogenic carbon as calculated by Lauvset et al. (2016) was added or subtracted to correct the data to the reference year of the climatology according to:

$$TCO_2^{year_2} = TCO_2^{year_1} - C_{ant_{2002}} [(1 + 0.0191)^{(year_1-2002)} - (1 + 0.0191)^{year_2-2002}] \quad (2)$$

where $TCO_2^{year_2}$ is the TCO_2 corrected to $year_2$, which is the reference year of the climatology, $TCO_2^{year_1}$ is the TCO_2 measured in $year_1$, $C_{ant_{2002}}$ is the anthropogenic carbon for 2002 and 0.0191 is the annual increase rate derived from the scaling factor determined by Gruber et al. (2019) for the global ocean between 1994 and 2007.

We compared our climatology with previously published climatologies of TCO₂. The surface monthly climatology created by Takahashi et al. (2014) was used to assess the spatiotemporal differences in the surface layer. The annual climatology of Lauvset et al. (2016) was used to evaluate the spatial differences in the deeper parts of the ocean. For the comparisons, the climatologies of Takahashi et al. (2014) and Lauvset et al. (2016) were adjusted to the year 1995 subtracting the anthropogenic carbon (C_{ant}) of Lauvset et al. (2016) as in the Eq. (2).

Finally, a surface climatology of pCO₂ was computed from the TCO₂ climatology of the present study and the A_T climatology of Broullón et al. (2019) to assess the potential of computing climatologies of other variables of the seawater CO₂ system. For comparison, the updated monthly pCO₂ climatology from Landschützer et al. (2016) (Landschützer et al., 2017, last access: 30 July 2019) was used. The values between 1981 and 2010 were averaged to obtain the climatological year 1995. The variable selected from Landschützer et al. (2017) was that labeled as spco2_raw (sea surface pCO₂) in the netCDF file.

It should be noted that the RMSE and the bias were obtained for all the comparisons, the last statistic being computed as the difference between the measured (or computed by the method to compare) TCO₂ and the one obtained with the neural network of the present study.

3. Results

3.1 Neural network analysis

Following the established criteria to obtain the optimal number of neurons, the configuration with 128 neurons in the hidden layer was selected. From the ten networks trained with this number of neurons for each approach (NNGv2LDEO and NNGv2QCLDEO), the ones with the lowest influence of the position input variables were selected. These two networks present a similar RMSE in both training and test datasets, showing there is no overfitting. Because in Gv2QC both NNGv2LDEO and NNGv2QCLDEO produce the same global RMSE (6.1 μmol kg⁻¹), it is likely that the Gv2 dataset contains high-quality measurements and the possible errors on the non-QC data of this dataset are clearly avoided by the network; otherwise NNGv2LDEO should have a higher RMSE in the test dataset than NNGv2QCLDEO because of an overfitting of the errors in the Gv2 dataset. The same holds for the LDEO dataset. The network properly fitted TCO₂ derived from LDEO, since it does not significantly increase the global RMSE relative to a network only trained with Gv2. Therefore, we decided to continue with NNGv2LDEO only since it has fitted more relationships between variables (e.g., Gv2 has more data points than Gv2QC in the Mediterranean Sea) providing a more robust fitting. For this network, the influence of each input variable on the computed TCO₂ is depicted in Fig. S2. The position variables together (latitude, longitude, longitude and depth) have no more than 30% influence, allowing biogeochemical variables to be the main ones responsible for the variability of TCO₂. Furthermore, the input variable year has an influence lower than 5%. This is probably responsible for capturing the positive interannual trend due to the TCO₂ increase derived from anthropogenic emissions of CO₂ to the atmosphere (see Sect. 3.2).

The global RMSE is quite low for the Gv2 dataset and for the LDEO dataset (Fig. 2). The measured and the computed data are highly correlated (Fig. 2) and the bias is negligible in both datasets. The higher
290 RMSE in the LDEO dataset likely results from the higher variability of TCO₂ in the surface layer and from uncertainties in its calculation from pCO₂.

The RMSE by area and depth for NNGv2LDEO and CANYON-B in Gv2QC is shown in Table 2. The highest errors for the two methods are in the 0-50 m layer for the Gv2QC dataset and the LDEO dataset. These errors get smaller with increasing depth for all areas and the depth-weighted RMSE of the two
295 methods is not significantly different below 50 m. In the LDEO dataset, NNGv2LDEO produces a lower error than CANYON-B, except for two areas: East GIN (Greenland, Iceland and Norwegian) Seas and the Bengal Basin (Table 2), although there are only 9 and 13 data points, respectively, in each area. Interestingly, CANYON-B is able to reproduce the TCO₂ data derived from the complete LDEO dataset with a lower error than the one it obtains for the complete Gv2QC dataset in the surface ocean (RMSE
300 LDEO: 16.4 μmol kg⁻¹; RMSE Gv2QC (0-5 m): 17.8 μmol kg⁻¹), supporting the approach of computing reliable TCO₂ values from the pCO₂ of LDEO and the A_T computed with NNGv2 (Broullón et al., 2019), since CANYON-B was not trained with the LDEO database. A similar result was obtained for NNGv2LDEO but with a higher difference between the two errors (RMSE LDEO: 11.4 μmol kg⁻¹; RMSE Gv2QC (0-5m): 17.1 μmol kg⁻¹). Finally, the surface RMSE towards LDEO data of NNGv2LDEO is clearly
305 lower than that of CANYON-B. This shows the value of including pCO₂ derived surface TCO₂ among the training data, through which there are more fitted relations in our new method.

For data from Gv2 where no QC was performed for at least one of the variables used in the present study (Gv2noQC), the RMSE also decreases with increasing depth: <50 m: 22.5 μmol kg⁻¹; 50-200 m: 9.8 μmol kg⁻¹; 200-500 m: 7 μmol kg⁻¹; 500-1000 m: 5.4 μmol kg⁻¹; >1000 m: 5.4 μmol kg⁻¹. Thus, the error in
310 Gv2noQC is similar to that in the areas with the highest error in Gv2QC (Table 2; except in Beaufort Sea, where the error is considerably higher). However, the higher error in Gv2noQC is mainly caused by the samples located in the Arctic Ocean, since cruises in the Atlantic and Pacific oceans are modeled with a very low error. Therefore, using Gv2noQC does not imply the introduction of low-quality data in our study, otherwise the network would not compute TCO₂ with low errors in Gv2QC because of an overfitting of the
315 possible low-quality data that Gv2noQC could contain.

In general, the highest differences between measured and estimated TCO₂ occurs in the high latitude surface oceans (Figs. 3 and 4). In Gv2, 40% of the samples with differences beyond ±3RMSE (3 times RMSE; threshold selected to refer samples with large residuals) are in latitudes greater than 70° N. In the LDEO dataset, 39% of the samples with differences beyond ±3RMSE are from latitudes south of 70° S. These
320 samples where RMSE is high are 7.5% of the total north of 70° N in Gv2 and 42% of the total south of 70° S in LDEO. The samples with low salinities have the highest errors (Fig. 4). 41.5% of the samples in Gv2 and 43% in LDEO with differences beyond ±3RMSE have salinities below 33. Furthermore, in the LDEO dataset, the number of samples with residuals beyond ±3RMSE increases with increasing standard deviation of both pCO₂ and salinity in the monthly averaging in each pixel in the LDEO subset (Fig. S3). This result
325 shows the difficulty of modeling areas with a high sub-monthly variability in pCO₂ and salinity and supports

the exclusion of the averaged LDEO data with a high standard deviation since it could cause the network to interpret the sub-monthly variability as monthly variability – note that the purpose of this study is to capture the monthly variability.

330 Like for modeling A_T (Takahashi et al., 2014; Broullón et al., 2019), the Arctic Ocean is one of the regions with the highest RMSE of neural network estimated TCO_2 . The major Arctic rivers contribute with TCO_2 concentrations ranging between 400 and 3600 $\mu\text{mol kg}^{-1}$ (estimated by Tank et al., 2012), derived mainly from carbonated rocks in the watersheds. Other areas like the Okhotsk Sea also show a high RMSE (Table 2 and Fig. 3), probably because of the high riverine input of TCO_2 (Watanabe et al., 2009). An input variable accounting for the contribution of the rivers to the TCO_2 pool would improve the neural network
335 performance in areas like these, but is not available.

The errors of the pCO_2 computed in LDEO with TCO_2 from NNGv2LDEO and A_T from NNGv2 (Broullón et al., 2019) are similar to the errors obtained by Landschützer et al. (2014) for the SOCAT database in some of the areas (10-16 μatm , Table 2). This result shows the potential of computing pCO_2 values with neural networks trained for other variables of the seawater CO_2 system, at least in some ocean regions. The
340 global error of the pCO_2 in the LDEO dataset is clearly higher than that obtained by Landschützer et al. (2014) for the SOCAT dataset (22 vs. 12 μatm , respectively), although the critical areas are mainly the same (Fig. S4): equatorial Pacific upwelling system, Arctic and subarctic waters around the Alaska Peninsula, the Southern Ocean, the Gulf Stream and the North Atlantic Current. At this point, the following should be considered: 1) the pCO_2 computed in the present study derives from A_T and TCO_2 and not from
345 specific modeling for pCO_2 , and therefore, it contains errors associated to this computation ($\sim 6 \mu\text{atm}$; Millero, 1995) and to the neural network estimates of A_T and TCO_2 ; 2) the present study includes the Arctic region where the highest errors occur (Table 2; Beaufort Sea and High Arctic areas); and 3) there is a longer temporal range in the present study (1973-2016). The analysis of Landschützer et al. (2014) in the LDEO dataset for data that differs from SOCAT shows a global error higher than the one obtained in the present
350 study for all LDEO data between 1998 and 2011 (25.9 vs. 21.3 μatm , respectively). The error between 40° S-40° N is similar in the two studies (Landschützer et al. (2014): 16.5 μatm ; NNGv2LDEO: 16.4 μatm). Although it is not the main objective of this work, these two last results show how NNGv2LDEO and NNGv2 (Broullón et al., 2019) have the potential to compute pCO_2 values between 40° S-40° N with similar errors as the method with the lower error in the pCO_2 modeling to obtain a climatology and with lower
355 errors in high latitudes, for the LDEO dataset; even taking into account the inclusion of the critical area of the Arctic in the computation of the error of the pCO_2 from the present study (it is not included in Landschützer et al., 2014) and the higher amount of data from high latitudes in the present study (15479 vs. 3799).

3.2 Time-series validation

360 The good generalization of the network in the test dataset containing data from Gv2 and LDEO by the similar RMSE that the one reached in the training set is also evidenced through independent time-series data (Table 3). Except for KERFIX, where the number of data points is very low and Olsen et al. (2019)

suggested an adjustment to the original data of $-39 \mu\text{mol kg}^{-1}$, TCO_2 computed using NNGv2LDEO and CANYON-B at the time-series locations are characterized by low errors and biases (Table 3).
365 NNGv2LDEO computes TCO_2 with a lower RMSE and bias than CANYON-B for most of the time-series stations (Table 3). CANYON-B reaches a lower RMSE in HOT ALOHA SURFACE and ESTOC than NNGv2LDEO, but the bias is considerably higher in these time series for CANYON-B.

The seasonal variability is well captured by NNGv2LDEO showing its great potential to design a monthly climatology. In the surface layer, where the seasonal variability is the highest, the computed values are
370 strongly correlated with the measured TCO_2 in all the time series (Fig. 5). In addition, the high correlation holds for all depths (Table S1). The location of the time series in different oceanographic regimes allows to complement the good TCO_2 computation by NNGv2LDEO already shown in the previous independent sets in almost any region of the ocean.

Assessing the potential of neural networks to obtain values of other variables of the seawater CO_2 system in the time series, pCO_2 calculated with A_T from NNGv2 (Broullón et al., 2019) and TCO_2 from NNGv2LDEO compared quite well with pCO_2 as measured or calculated from A_T and TCO_2 at the time-series stations (Table 4). Except for BATS, the pCO_2 obtained in the present study has a lower error than that reported by Landschützer et al. (2014) (Table 4). In contrast, the bias in the present study is higher, except for ESTOC. Considering the error involved in the calculation of pCO_2 from A_T and TCO_2 ($\sim 6 \mu\text{atm}$;
380 Millero, 1995) and the error in the computed A_T and TCO_2 with the neural networks (Table 4), our results demonstrate again the ability of NNGv2 and NNGv2LDEO to calculate other variables of the seawater CO_2 system with a relatively low error.

Using NNGv2LDEO, it is also possible to reproduce the secular trends in TCO_2 . Using seasonal detrending to enhance the multi-annual changes, similar trends in the longer time series are found for the measured
385 TCO_2 and the neural network computed TCO_2 (Table 5). The same holds for pCO_2 (Table 5), although at the IRMINGER site the trend obtained from the neural network generated data is significantly lower than that from measured data. The neural networks seem to capture the anthropogenic influence in the seawater CO_2 system and thus the ocean acidification process (Fig. 6). Furthermore, using NNGv2LDEO increases the amount of TCO_2 data where the various inputs were measured but not TCO_2 itself. This allows for
390 evaluation of high frequency changes (Fig. 6) and for calculation of interannual trends with a low error (as temporal sampling biases are reduced).

3.3 Climatology

Using NNGv2LDEO we have demonstrated its ability to compute TCO_2 values with low errors and, especially, to capture the monthly variability of this variable. In addition, the climatologies of the input
395 variables used to create the climatology of TCO_2 have been satisfactorily evaluated previously for the construction of an A_T climatology (Broullón et al., 2019). Considering these results, a monthly climatology of TCO_2 is obtained by passing the input climatologies through NNGv2LDEO.

The spatial distribution of the surface annual mean climatology of TCO₂ (Fig. 7a) is similar to two recent climatologies: those of Takahashi et al. (2014) and Lauvset et al. (2016). The largest surface TCO₂ concentrations occur in the Southern Ocean, subpolar North Atlantic, Nordic Seas and Mediterranean Sea (note that the latter is not included in these other climatologies). In general, surface TCO₂ decreases from high to low latitudes. The Indian and the Pacific oceans are characterized by lower concentrations of TCO₂ at higher latitudes than the Atlantic, the latter being the ocean with the highest surface TCO₂ by area. TCO₂ increases with depth in all oceans, in particular in the upwelling regions, where this increase is expanded eastwards with depth (Fig. 7b and video in <http://dx.doi.org/10.20350/digitalCSIC/10551>). Depending on the area, the values reach a maximum at certain intermediate depths and below it the concentration gradually decreases or remains almost constant (Fig. S5).

The largest seasonal variability occurs at the surface in high latitudes, in the Pacific upwelling region, the equatorial African coasts and in the area under influence of the Amazon River (Fig. 8a). At depth, the seasonal variability decreases, except for the Pacific upwelling region where it increases and moves progressively northward between 30 and 150 m (Fig 8b). This increase is correlated with the high seasonal variability of the climatologies of nutrients, oxygen and temperature at these depths. Czeschel et al. (2012) also showed an increase in the subsurface variability of oxygen from measured profiles. Similar increases also occur in the Indian Ocean north of 20° S between 50 and 100 m and in the equatorial Atlantic Ocean in the same depth range. At 1500 m level, the seasonal variability is below 10 μmol kg⁻¹ in most of the ocean (Fig. 8c). This last result shows that an annual climatology below 1500 m is sufficient.

Although the surface patterns of the annual mean of the TCO₂ climatology are very similar to those of the other recent climatologies (Takahashi et al., 2014; Lauvset et al., 2016), differences do occur. The annual mean climatology of the present study is closest to that of Takahashi et al. (2014) (Table 6). The largest differences between these two climatologies are located in the Arctic, North Pacific, Peru upwelling area, western South Pacific and the area of influence of the Antarctic Circumpolar Current (Fig. S6a). The Atlantic and the Indian oceans do not show significant differences. Our climatology shows more deviations to that of Lauvset et al. (2016), compared in the grid of Takahashi et al. (2014) (Table 6). The highest differences are found in the North Pacific, around Antarctica, Nordic Seas, South and North Atlantic and in several less localized areas around the oceans (Fig. S6b). When the climatology of Takahashi et al. (2014) is compared to that of Lauvset et al. (2016), the differences are even higher (Table 6) and the critical areas are the same of those of the previous comparison. Although it is clear that discrepancies between the three climatologies derive from the different methods used, the higher similarity between ours and the one of Takahashi et al. (2014) is probably due to the influence of the same source used to create them, the World Ocean Atlas.

The comparison of our climatology with that of Lauvset et al. (2016) at the 33 depth levels of Lauvset et al. (2016) shows a reduction of the RMSE with depth. Between 0 and 1000 m, the RMSE is reduced from ~32 to 7 μmol kg⁻¹ (Table S2) (note the higher RMSE at surface compared to one obtained for the grid of Takahashi et al. (2014) because of the inclusion of areas which are not included in the latter's grid, and the difficulty of modeling TCO₂ in some areas, like the Arctic and the Mediterranean Sea). This reduction with

depth is probably due to the reduction of the variability in most of the ocean below the surface. The surface values in Lauvset et al. (2016) are likely characteristic from months in which most of the sampling was carried out. Because of the lower variability of TCO₂ at depth, the values are closer to the annual mean and therefore the two compared climatologies are more similar at depth than in surface depth levels. Below
440 1000 m, the differences between the two climatologies are not significant, with a RMSE around 5 μmol kg⁻¹ and a bias around 0.5 μmol kg⁻¹ at each depth level (Table S2).

Our monthly climatology shows a high correspondence with that of Takahashi et al. (2014), although the RMSE values show that there are also large differences in certain areas (Table 7). These areas are mainly the same of those in the comparison of the annual mean climatologies, but some other small regions with
445 high differences appear for each month all through the ocean (Fig. S7).

Unfortunately, the uncertainty of the TCO₂ climatology cannot be assessed globally and robustly. As Broullón et al. (2019) stated, the unavailability of an uncertainty field associated to the WOA13 objectively analyzed climatologies does not allow to perform a proper global uncertainty assessment. Therefore, the analysis is relegated to the areas where repeated sampling of TCO₂ has been carried out monthly over a
450 long period, that is, the HOT ALOHA and BATS time-series stations. The climatology of TCO₂ from NNGv2LDEO is consistent with the monthly climatological values at these two places (Fig. 9). In general, the profiles from the TCO₂ climatology are within the variability range (shadow area in Fig. 9) of the monthly averaged measured data for each depth level. In the upper 30 m of the water column, the climatology of TCO₂ differs from the measured BATS data from May to August. This difference is mainly
455 explained by the surface error of the network showed for this time series in Fig. 5a, where the computed TCO₂ decreases from maximum to minimum sooner than the measured TCO₂. For HOT ALOHA, the RMSE of the profiles of the TCO₂ climatology oscillates between 3.6 and 9.2 μmol kg⁻¹ with a mean value of 6.3 μmol kg⁻¹ (bias range: -3.8 to 1.2 μmol kg⁻¹; mean bias: -1.4 μmol kg⁻¹). At BATS, the RMSE is lower than for HOT ALOHA: 1.1 to 8.5 μmol kg⁻¹ with a mean value of 4.4 μmol kg⁻¹ (bias range: -1.4 to
460 7.6 μmol kg⁻¹; mean bias: -2.5 μmol kg⁻¹). Furthermore, the seasonal variability of the TCO₂ climatology is quite similar to that of the measured data at BATS and HOT ALOHA (Fig. S8). Although in other time series there are not enough measured data to obtain climatological values, these pseudo climatological values also correlate very well with the TCO₂ climatology (data not shown). These results suggest that the climatology is robust in different oceanographic regimes and adequately captures the seasonal cycle of
465 TCO₂.

It has been demonstrated in this study that pCO₂ and possibly other variables of the seawater CO₂ system can be computed from A_T and TCO₂ derived from neural networks with a relatively low error in different datasets (LDEO in Sect. 3.1 and time series in Sect. 3.2). The pCO₂ climatology (Fig. S9) computed from the TCO₂ climatology of the present study and the A_T climatology of Broullón et al. (2019) is very similar
470 to that of Landschützer et al. (2017). The differences between the annual mean climatology of the two studies are below 15 μatm in most of the ocean (RMSE: 8.3 μatm; bias: 2.9 μatm; r²: 0.82). The differences above this threshold are mainly located in the Pacific equatorial upwelling system, the east part of the South Pacific Gyre, Nordic Seas, Labrador Sea, Atlantic section of the Southern Ocean, Bay of Bengal and the

475 waters surrounding the east margin of Asia (Fig. S10). In most of these areas, both methods have the greatest errors (Figs. 2 and 4 in Landschützer et al., 2014 and Fig. S4 of the present study).

480 On a monthly basis, the RMSE between the two pCO₂ climatologies is between 13.6 and 15.6 µatm and the correlation is lower than for the annual mean comparison (r^2 : 0.55-0.72 vs 0.82). The areas with the higher differences are the same as in the annual comparison but other small regions appear along the ocean month by month (Fig. S11). Furthermore, the seasonal variability in the two climatologies matches in a great extension of the ocean, although there are areas with notable differences (Fig. S12). In general, the pCO₂ climatology is quite similar to that of Landschützer et al. (2017) and this result contributes to show that both the TCO₂ climatology of the present study and the A_T climatology of Broullón et al. (2019) are mostly robust and suggest that climatologies of other seawater CO₂ system variables can be confidently computed.

485 **4 Data availability**

The climatologies of TCO₂ and pCO₂ and NNGv2LDEO designed in this study are available at the data repository of the Spanish National Research Council (CSIC; <http://dx.doi.org/10.20350/digitalCSIC/10551>, Broullón et al., 2020).

5 Conclusions

490 We presented a tool for computing TCO₂ in the global ocean. Compared to previous methods, the uncertainties in such computations have been reduced. Including two updated datasets containing thousands of measurements of inorganic carbon variables across the ocean in the training of the neural network, we were able to capture a wide range of variability of TCO₂. The low errors obtained in independent subsets as in time-series stations, are further evidence of the potential of the network in computing TCO₂.

495 Our global monthly climatology created with a neural network is the first that covers the oceans from the surface to the abyss at such temporal resolution. In addition to the accuracy of the network, the low uncertainty of the climatology in different regions and its usefulness in creating climatologies of other seawater CO₂ chemistry variables (i.e. pCO₂) show its robustness. Therefore, we present the global climatology of TCO₂ to the scientific community to complement the recently designed climatology of A_T by Broullón et al. (2019) for its use in the initialization and evaluation of models or any other analysis related to the carbon cycle.

6 Author contributions

DB, FFP and AV designed the study. The manuscript was written by DB and revised and discussed by all the authors. The dataset of the climatology and the neural network were created by DB.

505 **7 Competing interests**

The authors declare that they have no conflict of interest.

8 Acknowledgements

The authors want to thank the comments of the three referees to improve the study. The paper is dedicated to Taro Takahashi, who immensely contributed to the ocean's role in the carbon cycle and passed away in
510 December 2019.

9 Financial support

This research was supported by Ministerio de Educación, Cultura y Deporte (FPU grant FPU15/06026), Ministerio de Economía y Competitividad through the ARIOS (CTM2016-76146-C3-1-R) project co-funded by the Fondo Europeo de Desarrollo Regional 2014-2020 (FEDER) and EU Horizon 2020 through
515 the AtlantOS project (grant agreement 633211). Are Olsen was supported by the Norwegian Research Council through ICOS (245927). Mario Hoppema was partly supported by European Union's Horizon 2020 program under grant agreement no. 821001 (SO-CHIC).

10 References

Aumont, O., Ethé, C., Tagliabue, A., Bopp, L. and Gehlen, M.: PISCES-v2: An ocean biogeochemical
520 model for carbon and ecosystem studies, *Geosci. Model Dev.*, 8(8), 2465–2513, doi:10.5194/gmd-8-2465-2015, 2015.

Bakker, D. C. E., Pfeil, B., Landa, C. S., Metzl, N., O'Brien, K. M., Olsen, A., Smith, K., Cosca, C., Harasawa, S., Jones, S. D., Nakaoka, S. I., Nojiri, Y., Schuster, U., Steinhoff, T., Sweeney, C., Takahashi, T., Tilbrook, B., Wada, C., Wanninkhof, R., Alin, S. R., Balestrini, C. F., Barbero, L., Bates, N. R., Bianchi, A. A., Bonou, F., Boutin, J., Bozec, Y., Burger, E. F., Cai, W. J., Castle, R. D., Chen, L., Chierici, M., Currie, K., Evans, W., Featherstone, C., Feely, R. A., Fransson, A., Goyet, C., Greenwood, N., Gregor, L., Hankin, S., Hardman-Mountford, N. J., Harlay, J., Hauck, J., Hoppema, M., Humphreys, M. P., Hunt, C. W., Huss, B., Ibáñez, J. S. P., Johannessen, T., Keeling, R., Kitidis, V., Körtzinger, A., Kozyr, A., Krasakopoulou, E., Kuwata, A., Landschützer, P., Lauvset, S. K., Lefèvre, N., Lo Monaco, C., Manke, A.,
525 Mathis, J. T., Merlivat, L., Millero, F. J., Monteiro, P. M. S., Munro, D. R., Murata, A., Newberger, T., Omar, A. M., Ono, T., Paterson, K., Pearce, D., Pierrot, D., Robbins, L. L., Saito, S., Salisbury, J., Schlitzer, R., Schneider, B., Schweitzer, R., Sieger, R., Skjelvan, I., Sullivan, K. F., Sutherland, S. C., Sutton, A. J., Tadokoro, K., Telszewski, M., Tuma, M., Van Heuven, S. M. A. C., Vandemark, D., Ward, B., Watson, A. J. and Xu, S.: A multi-decade record of high-quality fCO₂ data in version 3 of the Surface Ocean CO₂
535 Atlas (SOCAT), *Earth Syst. Sci. Data*, 8(2), 383–413, doi:10.5194/essd-8-383-2016, 2016.

Bates, N. R., Best, M. H. P., Neely, K., Garley, R., Dickson, A. G. and Johnson, R. J.: Detecting anthropogenic carbon dioxide uptake and ocean acidification in the North Atlantic Ocean, *Biogeosciences*, 9(7), 2509–2522, doi:10.5194/bg-9-2509-2012, 2012.

Bauer, J. E., Cai, W. J., Raymond, P. A., Bianchi, T. S., Hopkinson, C. S. and Regnier, P. A. G.: The
540 changing carbon cycle of the coastal ocean, *Nature*, 504(7478), 61–70, doi:10.1038/nature12857, 2013.

- Beale, M. H., Hagan, T. M., and Demuth, H. B.: Deep Learning Toolbox™, User's Guide, Release 2018a, The MathWorks, Inc., Natick, Massachusetts, United States, available at: https://es.mathworks.com/help/pdf_doc/deeplearning/nnet Ug.pdf (last access: 20 August 2018), 2018.
- 545 Bittig, H. C., Steinhoff, T., Claustre, H., Fiedler, B., Williams, N. L., Sauzède, R., Körtzinger, A. and Gattuso, J.-P.: An Alternative to Static Climatologies: Robust Estimation of Open Ocean CO₂ Variables and Nutrient Concentrations From T, S, and O₂ Data Using Bayesian Neural Networks, *Front. Mar. Sci.*, 5,328, doi:10.3389/fmars.2018.00328, 2018.
- 550 Boyer, T.P., J. I. Antonov, O. K. Baranova, C. Coleman, H. E. Garcia, A. Grodsky, D. R. Johnson, R. A. Locarnini, A. V. Mishonov, T.D. O'Brien, C.R. Paver, J.R. Reagan, D. Seidov, I. V. Smolyar, and M. M. Zweng, 2013: World Ocean Database 2013, NOAA Atlas NESDIS 72, S. Levitus, Ed., A. Mishonov, Technical Ed.; Silver Spring, MD, 209 pp., <http://doi.org/10.7289/V5NZ85MT>, 2013.
- 555 Broullón, D., Pérez, F. F., Velo, A., Hoppema, M., Olsen, A., Takahashi, T., Key, R. M., Tanhua, T., González-Dávila, M., Jeansson, E., Kozyr, A. and van Heuven, S. M. A. C.: A global monthly climatology of total alkalinity: a neural network approach, *Earth Syst. Sci. Data*, 11(3), 1109–1127, doi:10.5194/essd-11-1109-2019, 2019.
- Broullón, D., Pérez, F. F., Velo, A., Hoppema, M., Olsen, A., Takahashi, T., Key, M., Tanhua, T., Santana-Casiano, J.M. and Kozyr, A.: A global monthly climatology of oceanic total dissolved inorganic carbon: a neural network approach (Discussions version) [Dataset], <http://dx.doi.org/10.20350/digitalCSIC/10551>, 2020.
- 560 Butenschön, M., Clark, J., Aldridge, J. N., Icarus Allen, J., Artioli, Y., Blackford, J., Bruggeman, J., Cazenave, P., Ciavatta, S., Kay, S., Lessin, G., Van Leeuwen, S., Van Der Molen, J., De Mora, L., Polimene, L., Saille, S., Stephens, N. and Torres, R.: ERSEM 15.06: A generic model for marine biogeochemistry and the ecosystem dynamics of the lower trophic levels, *Geosci. Model Dev.*, 9(4), 1293–1339, doi:10.5194/gmd-9-1293-2016, 2016.
- 565 Carter, B. R., Feely, R. A., Williams, N. L., Dickson, A. G., Fong, M. B. and Takeshita, Y.: Updated methods for global locally interpolated estimation of alkalinity, pH, and nitrate, *Limnol. Oceanogr. Methods*, 16(2), 119–131, doi:10.1002/lom3.10232, 2018.
- 570 Ciais, P., Sabine, C., Bala, G., Bopp, L., Brovkin, V., Canadell, J., Chhabra, A., DeFries, R., Galloway, J., Heimann, M., Jones, C., Quéré, C. Le, Myneni, R., Piao, S. and Thornton, P.: Carbon and Other Biogeochemical Cycles, in *Climate Change 2013 - The Physical Science Basis*, edited by Intergovernmental Panel on Climate Change, pp. 465–570, Cambridge University Press, Cambridge., 2013.
- Czeschel, R., Stramma, L. and Johnson, G. C.: Oxygen decreases and variability in the eastern equatorial Pacific, *J. Geophys. Res. Ocean.*, 117(C11), C11019, doi:10.1029/2012JC008043, 2012.

- 575 Dickson, A. G.: Thermodynamics of the dissociation of boric acid in synthetic seawater from 273.15 to 318.15 K, *Deep Sea Res. Part A.*, 37(5), 755–766, doi:10.1016/0198-0149(90)90004-F, 1990.
- Dickson, A. G. and Millero, F. J.: A comparison of the equilibrium constants for the dissociation of carbonic acid in seawater media, *Deep Sea Res. Part A*, 34(10), 1733–1743, doi:10.1016/0198-0149(87)90021-5, 1987.
- 580 Doi, T., Osafune, S., Sugiura, N., Kouketsu, S., Murata, A., Masuda, S. and Toyoda, T.: Multidecadal change in the dissolved inorganic carbon in a long-term ocean state estimation, *J. Adv. Model. Earth Syst.*, 7(4), 1885–1900, doi:10.1002/2015MS000462, 2015.
- Doney, S. C., Fabry, V. J., Feely, R. A. and Kleypas, J. A.: Ocean Acidification: The Other CO₂ Problem, *Ann. Rev. Mar. Sci.*, 1(1), 169–192, doi:10.1146/annurev.marine.010908.163834, 2009.
- 585 Dore, J. E., Lukas, R., Sadler, D. W., Church, M. J. and Karl, D. M.: Physical and biogeochemical modulation of ocean acidification in the central North Pacific, *Proc. Natl. Acad. Sci. U. S. A.*, 106(30), 12235–12240, doi:10.1073/pnas.0906044106, 2009.
- Fabry, V. J., Seibel, B. A., Feely, R. A., Fabry, J. C. O. and Fabry, V. J.: Impacts of ocean acidification on marine fauna and ecosystem processes, *ICES J. Mar. Sci.*, 65, 414–432, doi:10.1093/icesjms/fsn048, 2008.
- 590 Garcia, H. E., Locarnini, R. A., Boyer, T. P., Antonov, J. I., Baranova, O. K., Zweng, M. M., Reagan, J. R., and Johnson, D. R.: World Ocean Atlas 2013, Volume 3: Dissolved Oxygen, Apparent Oxygen Utilization, and Oxygen Saturation, edited by: Levitus, S. and Mishonov, A., Technical Ed., NOAA Atlas NESDIS 75, 27 pp., 2014.
- Gislefoss, J. S., Nydal, R., Slagstad, D., Sonninen, E. and Holmén, K.: Carbon time series in the Norwegian sea, *Deep. Res. Part I Oceanogr. Res. Pap.*, 45(2–3), 433–460, doi:10.1016/S0967-0637(97)00093-9, 1998.
- 595 González-Dávila, M., Santana-Casiano, J. M., Rueda, M. J. and Llinás, O.: The water column distribution of carbonate system variables at the ESTOC site from 1995 to 2004, *Biogeosciences*, 7(10), 3067–3081, doi:10.5194/bg-7-3067-2010, 2010.
- Goris, N., Tjiputra, J. F., Olsen, A., Schwinger, J., Lauvset, S. K. and Jeansson, E.: Constraining projection-based estimates of the future North Atlantic carbon uptake, *J. Clim.*, 31, 3959–3978, doi:10.1175/JCLI-D-17-0564.1, 2018.
- 600 Gruber, N., Clement, D., Carter, B. R., Feely, R. A., van Heuven, S., Hoppema, M., Ishii, M., Key, R. M., Kozyr, A., Lauvset, S. K., Monaco, C. Lo, Mathis, J. T., Murata, A., Olsen, A., Perez, F. F., Sabine, C. L., Tanhua, T. and Wanninkhof, R.: The oceanic sink for anthropogenic CO₂ from 1994 to 2007, *Science*, 363(6432), 1193–1199, doi:10.1126/science.aau5153, 2019.
- 605 Hendriks, I. E., Duarte, C. M. and Álvarez, M.: Vulnerability of marine biodiversity to ocean acidification: A meta-analysis, *Estuar. Coast. Shelf Sci.*, 86(2), 157–164, doi:10.1016/J.ECSS.2009.11.022, 2010.

- Hoegh-Guldberg, O. and Bruno, J. F.: The Impact of Climate Change on the World's Marine Ecosystems, *Science*, 328(5985), 1523–1528, doi:10.1126/science.1189930, 2010.
- 610 Jeandel, C., Ruiz-Pino, D., Gjata, E., Poisson, A., Brunet, C., Charriaud, E., Dehairs, F., Delille, D., Fiala, M., Fravallo, C., Carlos Miquel, J., Park, Y. H., Pondaven, P., Quéguiner, B., Razouls, S., Shauer, B. and Tréguer, P.: KERFIX, a time-series station in the Southern Ocean: A presentation, in *Journal of Marine Systems*, 17, 555–569., 1998.
- 615 Key, R. M., Kozyr, A., Sabine, C. L., Lee, K., Wanninkhof, R., Bullister, J. L., Feely, R. A., Millero, F. J., Mordy, C. and Peng, T. H.: A global ocean carbon climatology: Results from Global Data Analysis Project (GLODAP), *Global Biogeochem. Cycles*, 18(4), 1–23, doi:10.1029/2004GB002247, 2004.
- Key, R. M., Olsen, A., van Heuven, S., Lauvset, S. K., Velo, A., Lin, X., Schirnack, C., Kozyr, A., Tanhua, T., Hoppema, M., Jutterström, S., Steinfeldt, R., Jeansson, E., Ishi, M., Perez, F. F. and Suzuki, T.: Global Ocean Data Analysis Project, Version 2 (GLODAPv2), ORNL/CDIAC-162, NDP-093, doi:10.3334/CDIAC/OTG.NDP093_GLODAPv2, 2015.
- 620 Khatiwala, S., Tanhua, T., Mikaloff Fletcher, S., Gerber, M., Doney, S. C., Graven, H. D., Gruber, N., McKinley, G. A., Murata, A., Ríos, A. F. and Sabine, C. L.: Global ocean storage of anthropogenic carbon, *Biogeosciences*, 10(4), 2169–2191, doi:10.5194/bg-10-2169-2013, 2013.
- Kleypas, J. and Langdon, C.: Overview of CO₂-induced changes in seawater chemistry, *Proc. 9th Int. Coral Reef Symp. Bali.*, 2, 2000.
- 625 Körtzinger, A., Hedges, J. I. and Quay, P. D.: Redfield ratios revisited: Removing the biasing effect of anthropogenic CO₂, *Limnol. Oceanogr.*, 4, doi:10.4319/lo.2001.46.4.0964, 2001.
- Kroeker, K. J., Kordas, R. L., Crim, R., Hendriks, I. E., Ramajo, L., Singh, G. S., Duarte, C. M. and Gattuso, J.-P.: Impacts of ocean acidification on marine organisms: quantifying sensitivities and interaction with warming, *Glob. Chang. Biol.*, 19(6), 1884–1896, doi:10.1111/gcb.12179, 2013.
- 630 Landschützer, P., Gruber, N., Bakker, D. C. E. and Schuster, U.: Recent variability of the global ocean carbon sink, *Global Biogeochem. Cycles*, 28(9), 927–949, doi:10.1002/2014GB004853, 2014.
- Landschützer, P., Gruber, N. and Bakker, D. C. E.: Decadal variations and trends of the global ocean carbon sink, *Global Biogeochem. Cycles*, 30(10), 1396–1417, doi:10.1002/2015GB005359, 2016.
- 635 Landschützer, P., Gruber, N. and Bakker, D.C.E.: An updated observation-based global monthly gridded sea surface pCO₂ and air-sea CO₂ flux product from 1982 through 2015 and its monthly climatology (NCEI Accession 0160558). Version 2.2. NOAA National Centers for Environmental Information. Dataset. [2017-07-11], (last access: 15 July 2019), 2017
- Lauvset, S. K., Key, R. M., Olsen, A., Van Heuven, S., Velo, A., Lin, X., Schirnack, C., Kozyr, A., Tanhua, T., Hoppema, M., Jutterström, S., Steinfeldt, R., Jeansson, E., Ishii, M., Perez, F. F., Suzuki, T. and Watelet,

- 640 S.: A new global interior ocean mapped climatology: The $1^{\circ} \times 1^{\circ}$ GLODAP version 2, *Earth Syst. Sci. Data*, 8(2), 325–340, doi:10.5194/essd-8-325-2016, 2016.
- Lee, K., Wanninkhof, R., Feely, R. A., Millero, F. J. and Peng, T.-H.: Global relationships of total inorganic carbon with temperature and nitrate in surface seawater, *Global Biogeochem. Cycles*, 14(3), 979–994, doi:10.1029/1998GB001087, 2000.
- 645 Le Quéré, C., Buitenhuis, E. T., Moriarty, R., Alvain, S., Aumont, O., Bopp, L., Chollet, S., Enright, C., Franklin, D. J., Geider, R. J., Harrison, S. P., Hirst, A. G., Larsen, S., Legendre, L., Platt, T., Prentice, I. C., Rivkin, R. B., Sailley, S., Sathyendranath, S., Stephens, N., Vogt, M. and Vallina, S. M.: Role of zooplankton dynamics for Southern Ocean phytoplankton biomass and global biogeochemical cycles, *Biogeosciences*, 13(14), 4111–4133, doi:10.5194/bg-13-4111-2016, 2016.
- 650 Le Quéré, C., Andrew, R. M., Friedlingstein, P., Sitch, S., Hauck, J., Pongratz, J., Pickers, P. A., Korsbakken, J. I., Peters, G. P., Canadell, J. G., Arneeth, A., Arora, V. K., Barbero, L., Bastos, A., Bopp, L., Chevallier, F., Chini, L. P., Ciais, P., Doney, S. C., Gkritzalis, T., Goll, D. S., Harris, I., Haverd, V., Hoffman, F. M., Hoppema, M., Houghton, R. A., Hurtt, G., Ilyina, T., Jain, A. K., Johannessen, T., Jones, C. D., Kato, E., Keeling, R. F., Goldewijk, K. K., Landschützer, P., Lefèvre, N., Lienert, S., Liu, Z.,
- 655 Lombardozzi, D., Metzl, N., Munro, D. R., Nabel, J. E. M. S., Nakaoka, S., Neill, C., Olsen, A., Ono, T., Patra, P., Peregón, A., Peters, W., Peylin, P., Pfeil, B., Pierrot, D., Poulter, B., Rehder, G., Resplandy, L., Robertson, E., Rocher, M., Rödenbeck, C., Schuster, U., Schwinger, J., Séférian, R., Skjelvan, I., Steinhoff, T., Sutton, A., Tans, P. P., Tian, H., Tilbrook, B., Tubiello, F. N., van der Laan-Luijkx, I. T., van der Werf, G. R., Viovy, N., Walker, A. P., Wiltshire, A. J., Wright, R., Zaehle, S. and Zheng, B.: Global Carbon Budget 2018, *Earth Syst. Sci. Data*, 10(4), 2141–2194, doi:10.5194/essd-10-2141-2018, 2018.
- 660 Levenberg, K.: A method for the solution of certain non-linear problems in least squares., *Q. Appl. Math.*, II(2), 164–168, 1944.
- Locarnini, R. A., Mishonov, A. V., Antonov, J. I., Boyer, T. P., Garcia, H. E., Baranova, O. K., Zweng, M. M., Paver, C. R., Reagan, J. R., Johnson, D. R., Hamilton, M., and Seidov, D.: *World Ocean Atlas 2013, Volume 1: Temperature*, edited by: Levitus, S. and Mishonov, A., NOAA Atlas NESDIS 73, 40 pp., 2013.
- 665 Marquardt, D. W.: An Algorithm for Least-Squares Estimation of Nonlinear Parameters, *J. Soc. Ind. Appl. Math.*, 11(2), 431-441, 1963.
- Mehrbach, C., Culbertson, C. H., Hawley, J. E. and Pytkowicz, R. M.: Measurement of the apparent dissociation constants of carbonic acid in seawater at atmospheric pressure, *Limnol. Oceanogr.*, 18(6), 897–
- 670 907, doi:10.4319/lo.1973.18.6.0897, 1973.
- Millero, F. J.: Thermodynamics of the carbon dioxide system in the oceans, *Geochim. Cosmochim. Acta*, 59(4), 661–677, doi:10.1016/0016-7037(94)00354-O, 1995.

Millero, F. J.: The Marine Inorganic Carbon Cycle, *Chem. Rev.*, 107(2), 308–341, doi:10.1021/cr0503557, 2007.

675 Olafsson, J., Olafsdottir, S. R., Benoit-Cattin, A. and Takahashi, T.: The Irminger Sea and the Iceland Sea time series measurements of sea water carbon and nutrient chemistry 1983–2008, *Earth Syst. Sci. Data*, 2(1), 99–104, doi:10.5194/essd-2-99-2010, 2010.

Olden, J. D. and Jackson, D. A.: Illuminating the “black box”: a randomization approach for understanding variable contributions in artificial neural networks, *Ecol. Modell.*, 154, 135–150, doi:10.1016/S0304-3800(02)00064-9, 2002.

Olsen, A., Lange, N., Key, R. M., Tanhua, T., Álvarez, M., Becker, S., Bittig, H. C., Carter, B. R., Cotrim da Cunha, L., Feely, R. A., van Heuven, S., Hoppema, M., Ishii, M., Jeansson, E., Jones, S. D., Jutterström, S., Karlsen, M. K., Kozyr, A., Lauvset, S. K., Lo Monaco, C., Murata, A., Pérez, F. F., Pfeil, B., Schirnick, C., Steinfeldt, R., Suzuki, T., Telszewski, M., Tilbrook, B., Velo, A. and Wanninkhof, R.: GLODAPv2.2019 - an update of GLODAPv2, *Earth Syst. Sci. Data*, 11, 1437–1461, <https://doi.org/10.5194/essd-11-1437-2019>, 2019.

Orr, J. C., Fabry, V. J., Aumont, O., Bopp, L., Doney, S. C., Feely, R. A., Gnanadesikan, A., Gruber, N., Ishida, A., Joos, F., Key, R. M., Lindsay, K., Maier-Reimer, E., Matear, R., Monfray, P., Mouchet, A., Najjar, R. G., Plattner, G. K., Rodgers, K. B., Sabine, C. L., Sarmiento, J. L., Schlitzer, R., Slater, R. D., 690 Totterdell, I. J., Weirig, M. F., Yamanaka, Y. and Yool, A.: Anthropogenic ocean acidification over the twenty-first century and its impact on calcifying organisms, *Nature*, 437(7059), 681–686, doi:10.1038/nature04095, 2005.

Rumelhart, D. E., Hinton, G. E., and Williams, R. J.: Learning representations by back-propagating errors, *Nature*, 323, 533–536, <https://doi.org/10.1038/323533a0>, 1986.

695 Sabine, C. L., Key, R. M., Feely, R. A. and Greeley, D.: Inorganic carbon in the Indian Ocean: Distribution and dissolution processes, *Global Biogeochem. Cycles*, 16(4), 15-1-15-18, doi:10.1029/2002GB001869, 2002.

Sallée, J.-B., Matear, R. J., Rintoul, S. R. and Lenton, A.: Localized subduction of anthropogenic carbon dioxide in the Southern Hemisphere oceans, *Nat. Geosci.*, 5(8), 579–584, doi:10.1038/ngeo1523, 2012.

700 Sarmiento, J. L. and Gruber, N.: Sinks for Anthropogenic Carbon, *Phys. Today*, 55(8), 30–36, doi:10.1063/1.1510279, 2002.

Sauzède, R., Claustre, H., Pasqueron de Fommervault, O., Bittig, H. C., Gattuso, J.-P., Legendre, L. and Johnson, K. S.: Estimates of water-column nutrients concentration and carbonate system parameters in the global ocean: A novel approach based on neural networks, *Front. Mar. Sci.*, 4, 128, 705 doi:10.3389/fmars.2017.00128, 2017.

Schlitzer, R., Ocean Data View, available at: <http://odv.awi.de> (last access: 21 May 2018), 2016.

Takahashi, T., Sutherland, S. C., Chipman, D. W., Goddard, J. G. and Ho, C.: Climatological distributions of pH, pCO₂, total CO₂, alkalinity, and CaCO₃ saturation in the global surface ocean, and temporal changes at selected locations, *Mar. Chem.*, 164, 95–125, doi:10.1016/j.marchem.2014.06.004, 2014.

710 Takahashi, T., S.C. Sutherland and A. Kozyr.: Global Ocean Surface Water Partial Pressure of CO₂ Database: Measurements Performed During 1957-2016 (Version 2016). ORNL/CDIAC-161, NDP-088(V2015). Carbon Dioxide Information Analysis Center, Oak Ridge National Laboratory, U.S. Department of Energy, Oak Ridge, Tennessee, doi: 10.3334/CDIAC/OTG.NDP088(V2016), 2017

715 Tanhua, T., Bates, N. R. and Körtzinger, A.: The Marine Carbon Cycle and Ocean Carbon Inventories, in *International Geophysics*, vol. 103, edited by J. Siedler, G., Griffies, S., Gould, J. and Church, pp. 787–815, Academic Press., 2013.

720 Tank, S. E., Raymond, P. A., Striegl, R. G., McClelland, J. W., Holmes, R. M., Fiske, G. J. and Peterson, B. J.: A land-to-ocean perspective on the magnitude, source and implication of DIC flux from major Arctic rivers to the Arctic Ocean, *Global Biogeochem. Cycles*, 26(4), GB4018, doi:10.1029/2011GB004192, 2012.

van Heuven, S., D. Pierrot, J.W.B. Rae, E. Lewis, and D.W.R. Wallace: MATLAB Program Developed for CO₂ System Calculations. ORNL/CDIAC-105b. Carbon Dioxide Information Analysis Center, Oak Ridge National Laboratory, U.S. Department of Energy, Oak Ridge, Tennessee. https://doi.org/10.3334/CDIAC/otg.CO2SYS_MATLAB_v1.1, 2011.

725 Vázquez-Rodríguez, M., Touratier, F., Lo Monaco, C., Waugh, D. W., Padin, X. A., Bellerby, R. G. J., Goyet, C., Metzl, N., Ríos, A. F. and Pérez, F. F.: Anthropogenic carbon distributions in the Atlantic Ocean: data-based estimates from the Arctic to the Antarctic, *Biogeosciences*, 6(3), 439–451, doi:10.5194/bg-6-439-2009, 2009.

730 Wakita, M., Watanabe, S., Murata, A., Tsurushima, N. and Honda, M.: Decadal change of dissolved inorganic carbon in the subarctic western North Pacific Ocean, *Tellus B Chem. Phys. Meteorol.*, 62(5), 608–620, doi:10.1111/j.1600-0889.2010.00476.x, 2010.

Weiss, R. F., Jahnke, R. A. and Keeling, C. D.: Seasonal effects of temperature and salinity on the partial pressure of CO₂ in seawater, *Nature*, 300(5892), 511–513, doi:10.1038/300511a0, 1982.

735 Wu, Y., Hain, M. P., Humphreys, M. P., Hartman, S. and Tyrrell, T.: What drives the latitudinal gradient in open-ocean surface dissolved inorganic carbon concentration?, *Biogeosciences*, 16(13), 2661–2681, doi:10.5194/bg-16-2661-2019, 2019.

Yool, A., Popova, E. E. and Anderson, T. R.: MEDUSA-2.0: An intermediate complexity biogeochemical model of the marine carbon cycle for climate change and ocean acidification studies, *Geosci. Model Dev.*, 6(5), 1767–1811, doi:10.5194/gmd-6-1767-2013, 2013.

740 Zeebe and Wolf-Gladrow: CO₂ in seawater: Equilibrium, Kinetics, Isotopes, in Elsevier oceanography series, edited by D. Halpem, Elsevier Oceanography Series., 2001.

Zweng, M.M, J.R. Reagan, J.I. Antonov, R.A. Locarnini, A.V. Mishonov, T.P. Boyer, H.E. Garcia, O.K. Baranova, D.R. Johnson, D. Seidov, M.M. Biddle.: World Ocean Atlas 2013, Volume 2: Salinity. S. Levitus, Ed., A. Mishonov Technical Ed.; NOAA Atlas NESDIS 74, 39 pp., 2013.

745

Table 1. Differences between the methods used in the present study and in CANYON-B (Bittig et al., 2018).

	Bittig et al. (2018)	This study
Training technique	Bayesian regularization	Levenberg-Marquardt
Input variables	Temperature, salinity, oxygen, position and time	Temperature, salinity, oxygen, phosphate, nitrate, silicate, position and time
Datasets	GLODAPv2 (Olsen et al., 2016)	GLODAPv2.2019 (Olsen et al., 2019) LDEOv2016 (Takahashi et al., 2017)

750

Table 2. RMSE (bias) by area and depth for TCO₂ and pCO₂ computed with CANYON-B and NNGv2LDEO in Gv2QC and LDEO datasets. For each depth range, the RMSE (bias) in each area was weighted by the contribution of its data to the total. Units are micromoles per kilogram (μmol kg⁻¹) for TCO₂ and microatmospheres (μatm) for pCO₂.

	TCO ₂											pCO ₂		
	0-50 m				50-200 m		200-500 m		500-1000 m		>1000 m		0 m	
	LDEO (0 m)		Gv2QC		Gv2QC		Gv2QC		Gv2QC		Gv2QC		LDEO	
	NNGv2LDEO	CANYON-B	NNGv2LDEO	CANYON-B	NNGv2LDEO	CANYON-B	NNGv2LDEO	CANYON-B	NNGv2LDEO	CANYON-B	NNGv2LDEO	CANYON-B	NNGv2LDEO	CANYON-B
Areas defined in Takahashi et al. (2014)														
West GIN Seas	16.8 (7.6)	21.2 (18.1)	14.2 (-1.7)	15.3 (0.7)	6.4 (-0.6)	6.7 (0.3)	5.5 (-1.1)	6.8 (-0.5)	4.1 (0.9)	5 (1.3)	4 (0.8)	4.1 (0.8)	28.6 (17.2)	34.9 (35.2)

East GIN Seas	11.1 (14.1)	9.2 (5.6)	10.2 (1.6)	11.4 (1.3)	5.9 (0.5)	6.2 (2.9)	4.6 (-0.8)	5.2 (1.7)	3.5 (-0.6)	4 (2.3)	3.9 (-0.6)	3.7 (0.1)	17.3 (22.4)	15 (9.4)
High Arctic	13.3 (-8.3)	32.4 (13.7)	20.2 (-1.1)	24.1 (4.4)	11.4 (-0.1)	12.3 (1.7)	6.5 (0.1)	6.6 (-0.2)	6.8 (-0.1)	7.6 (0.6)	6.1 (-0.4)	6.2 (-1.1)	43 (-22.8)	79.1 (22.6)
Beaufort Sea	29.7 (0.8)	42 (10)	54 (0.1)	53.1 (1.3)	14.5 (-1.7)	13.3 (1.8)	8.1 (0.1)	9.2 (-1)	7.5 (2)	8.4 (-0.5)	6.5 (1.1)	7.2 (-2.1)	58.7 (6.7)	135.6 (5.3)
Labrador Sea	5.3 (0.6)	7.5 (2.7)	10.5 (-0.9)	11.6 (1.3)	5.4 (-0.2)	6.6 (1.6)	4.1 (-0.6)	4.3 (1.4)	3.5 (-0.1)	3.7 (1.5)	2.7 (0.2)	3.1 (1.6)	10.7 (1)	13.6 (4.5)
Subarctic Atlantic	11.7 (3.3)	14.6 (11.5)	9 (-2.3)	11.1 (1.5)	4.5 (0.1)	5.4 (1.9)	4.3 (0.1)	4.8 (0.3)	4.2 (0.1)	4.6 (0.4)	4 (-0.2)	4.3 (0)	21.9 (7.8)	26.7 (23.2)
North Atlantic Drift	11.1 (0.5)	12.9 (5.7)	13.3 (-1.3)	14.5 (0.5)	9.9 (0.7)	10.4 (0.5)	7.8 (0)	7.8 (-0.4)	4.3 (0.2)	4.5 (0.1)	3.5 (0.3)	3.6 (-0.1)	21 (1.4)	24.7 (10.3)
Central Atlantic	7.9 (-0.3)	9.6 (-1.2)	15.8 (0)	14.9 (0.3)	6.6 (0.2)	6.5 (1)	5.2 (-0.5)	5.1 (0.5)	4.6 (-0.1)	4.5 (0)	4.3 (0)	4.4 (0)	13.5 (-0.3)	17.4 (-2)
South Atlantic Transition Zone	7.7 (-1.3)	13.8 (-2.1)	7.2 (-0.9)	7.8 (0.3)	5.4 (0.8)	5.7 (0.1)	5.7 (1.1)	4.7 (0.7)	5 (-0.1)	4.8 (1)	4.3 (0.5)	4.2 (0.3)	14.6 (-2.7)	25 (-5.2)
Antarctic Atlantic	11.8 (1.4)	19.2 (20.9)	8.6 (-1.6)	10 (0.5)	4.6 (0)	5.4 (0.4)	3.5 (-0.1)	3.8 (0.3)	3.1 (0.1)	3.1 (0.3)	3.1 (0)	3.1 (0.3)	25.6 (4.9)	41.5 (50.9)
Kuroshio Alaska Gyre	10.9 (1.6)	12.3 (1.5)	8.5 (-0.9)	12.2 (2.4)	6.4 (0.9)	8.1 (0.3)	5 (0.3)	5.2 (1.1)	4.5 (0.6)	4.3 (0.3)	3.7 (0.4)	3.9 (0.3)	20.7 (3.7)	23.7 (3.4)
North Central Pacific	26.3 (-3.6)	34.5 (-9.6)	9.6 (0.2)	15 (3.4)	6.8 (0.5)	8.3 (0.4)	4.2 (0.3)	4.7 (0.5)	4 (-0.3)	4.1 (0.3)	3.4 (0.3)	3.8 (0)	46.7 (-0.4)	56.6 (-7)
Okhotsk Sea	- -	- -	23.1 (0.9)	16.4 (1.6)	11.3 (-1.2)	6.8 (-0.7)	6.3 (-2.3)	5.1 (-1.6)	5.2 (-4)	3.4 (-1.3)	4.1 (1.2)	3.5 (1.9)	- -	- -
Central Tropical North Pacific	8 (-1.3)	9.7 (-3.2)	7.9 (-0.9)	8.8 (0.5)	7.2 (0.5)	7.2 (1.2)	4.9 (-0.6)	5 (0.2)	4.3 (-0.4)	4.5 (0.5)	3.6 (-0.2)	3.8 (0.2)	14.2 (-2.1)	17.2 (-5.6)
Tropical East North Pacific	11.1 (-0.1)	14.5 (-4.5)	10.9 (0.9)	13.8 (-1.4)	5.9 (0.3)	8.5 (2.5)	2.6 (0.3)	3.4 (1.7)	2.1 (0)	2.1 (0.6)	2.4 (-0.2)	2.1 (-0.3)	20.8 (0.2)	28.2 (-8.8)
Panama Basin	12.5 (-0.7)	17.4 (0.7)	10.2 (-3.4)	9.5 (1.5)	6.5 (-2.7)	3.9 (-6.7)	4 (2.3)	5.8 (-1.2)	3.8 (0.8)	3.2 (1.4)	4.2 (0)	4.3 (2.8)	25.8 (-0.3)	38.8 (1.3)
Central South Pacific	10.1 (-2.1)	12.9 (-3.4)	10.3 (1.2)	10.9 (-0.7)	8.9 (0)	9.4 (0.2)	4.4 (-0.1)	4.5 (0.8)	3.8 (-0.1)	3.8 (-0.4)	3.3 (0)	3.5 (-0.1)	18.6 (-3)	24.3 (-5)
East Central South Pacific	10.7 (-1)	15.4 (-0.1)	10.6 (0.6)	15.2 (1.4)	6.9 (1.2)	7.5 (1.3)	4.1 (0.4)	2.8 (0.1)	3.8 (-0.5)	3.5 (-0.2)	3.3 (-0.6)	3 (0.3)	24.1 (-1.2)	34.2 (0.5)
Subpolar South Pacific	6.9 (1.2)	7.9 (-0.9)	5.8 (-0.7)	7.7 (2.4)	5 (0.4)	5.4 (0.6)	2.9 (0.9)	2.8 (1.7)	4.7 (-1)	4.8 (1.2)	4.1 (0.7)	4.4 (1)	13.7 (2.4)	16 (-2.2)
Antarctic Pacific	19.5 (1.9)	29.3 (4.9)	8.3 (-1.4)	7 (0.5)	3.6 (-0.5)	4.1 (0.5)	2.7 (-0.1)	3.3 (0.7)	2.6 (0.3)	2.9 (0.3)	2.6 (0.5)	2.1 (-0.1)	34.1 (7.7)	53.8 (14.9)
Main North Indian	10.8 (-1.8)	13 (-7.7)	10.5 (2.8)	12.9 (1.7)	8.1 (-0.1)	7.8 (0.5)	3.2 (0.7)	3.3 (0.9)	2.4 (-0.4)	2.6 (-0.4)	3.1 (-0.2)	3.7 (0.2)	19.8 (-2.8)	23.5 (-12.7)
Red Sea	18.3 (-13.9)	20.9 (-16.7)	12 (-4.3)	16.8 (-3.5)	9.4 (0.2)	8.7 (-3.7)	7.6 (-4.3)	7.9 (-5.1)	7.4 (1)	5.7 (-4.4)	3.3 (-1.3)	7.2 (-1.1)	28 (-21)	32.3 (-25.5)
Bengal Basin	6 (1.1)	3.7 (-5.5)	9.8 (-0.2)	7.4 (2)	7.4 (0.3)	6.4 (1.3)	2 (0.4)	2.1 (1.1)	1.9 (0.4)	2.1 (-0.2)	2 (-0.6)	2.2 (-0.4)	10.7 (1.4)	6.7 (-10.2)
Main South Indian	8.1	10.4	9.1	10	7.1	6.9	3.8	3.8	4.2	4.5	3.4	3.8	14	17.7

South Indian Transition	(-0.2)	(0.4)	(-0.1)	(1)	(0.3)	(0.6)	(-0.1)	(0.9)	(0.1)	(1.1)	(0.1)	(0.1)	(-0.1)	(0.9)
	8	9.4	5.3	5.3	4.1	4.4	4	3.7	3.9	3.4	3.4	3.7	16	18.8
Antarctic Indian	(-0.4)	(0.7)	(-1.7)	(-0.4)	(0.8)	(0.8)	(0)	(0.5)	(-0.2)	(0.3)	(-0.6)	(-0.9)	(-0.7)	(1.9)
	9.7	11.8	6	6.8	4.1	4.7	3	3.3	2.5	2.6	2.7	2.6	23.2	28.7
Cicumplar Southern Ocean	(1.1)	(5.9)	(-1.4)	(0.2)	(0.4)	(0.6)	(0.1)	(0.3)	(-0.3)	(0.3)	(0.3)	(0.5)	(3.9)	(15.3)
	15.9	24.5	7.6	8.2	4.4	4.9	3.1	3.4	2.9	2.9	2.9	2.7	30.7	48.9
Weighted	(0.9)	(9.8)	(-1.6)	(0.4)	(-0.2)	(0.3)	(-0.1)	(0.2)	(0)	(0.2)	(0.1)	(0.2)	(4.7)	(25.7)
	11.1	15	11	12.1	6.6	7	4.3	4.5	4	4.1	3.5	3.7	21.1	29.6
	(0)	(2.8)	(-0.5)	(0.8)	(0.2)	(0.8)	(-0.1)	(0.5)	(-0.1)	(0.3)	(0.1)	(0.2)	(1.3)	(7.5)

755 **Table 3. RMSE and bias between measured and computed TCO₂ concentrations in several time series. The comparison was done using only water samples where all the input variables for NNGv2LDEO and the TCO₂ were measured in the same water sample.**

Time series	Location	Time period	n	NNGv2LDEO		CANYON-B	
				RMSE (μmol kg ⁻¹)	Bias (μmol kg ⁻¹)	RMSE (μmol kg ⁻¹)	Bias (μmol kg ⁻¹)
BATS	31.7°N, 64.2°W	1988-2014	4121	7.7	0.1	7.7	-0.6
HOT ALOHA	22.8°N, 158°W	1988-2017	4054	5.4	-0.5	5.1	-2
HOT ALOHA SURF	22.8°N, 158°W	1988-2016	281	6.3	-1.6	5.8	-5.1
ESTOC	29.3°N, 15.5°W	1995-2008	1697	7.1	0.8	6.6	4.7
ICELAND	68°N, 12.7°W	1985-2013	1322	5.4	5.6	6.9	5.3
IRMINGER	64.3°N, 28°W	1991-2013	1086	4.8	3.3	7.5	6.6
K2	47°N, 160°E	1999-2008	615	3.6	1.3	6.3	2.4
KNOT	44°N, 155°E	1997-2008	1321	5.8	-0.8	7.2	-1.9
OWS	66°N, 2°E	2001-2007	803	6.8	-1	10.5	-4.7
KERFIX	50.4°S, 68.2°E	1992-1994	38	13.2	26.4	13.1	28.9

760 **Table 4. RMSE and bias between measured pCO₂ (and in some cases, computed from measured A_T and TCO₂ in time series where pCO₂ was not measured) and computed pCO₂ with A_T from NNGv2 (Broullón et al., 2019) and TCO₂ from NNGv2LDEO in several time series. The time period for pCO₂ from this study is the same as in Table 3. Consult Table 2 in Landschützer et al. (2014) for its time period. The depth range is 0-15 m. Only time series with more than 30 data points are included. RMSE and bias for computed A_T with NNGv2 (Broullón et al., 2019) and TCO₂ with NNGv2LDEO are included to show the errors in the variables used to compute TCO₂.**

Time series	pCO ₂				A _T		TCO ₂	
	NNGv2LDEO		Landschützer et al., 2014		NNGv2 (Broullón et al. 2019)		NNGv2LDEO	
	RMSE (μatm)	Bias (μatm)	RMSE (μatm)	Bias (μatm)	RMSE (μatm)	Bias (μatm)	RMSE (μatm)	Bias (μatm)
BATS	17.2	9.7	15.6	0.4	5.6	-1.7	10.1	4.4
HOT ALOHA SURF	10.3	-3.6	11.6	0.1	5.0	0.9	6.5	-1.6
ESTOC	10.6	2.7	14.5	-7.1	2.6	-2.7	5.3	-0.6
ICELAND	16	14.8	-	-	5.4	0.7	5.4	5.4
IRMINGER	13.1	-1.8	22.6	-1.1	7.0	-0.4	6.6	-1.1

K2	18.1	-3.2	27.8	-0.2	5.1	-0.5	5.7	-2.4
KNOT	20.8	8.6	-	-	6.6	-7.3	8.2	-2.5

765

Table 5. Long-term trends (seasonally detrended) of the measured and computed TCO₂ and pCO₂ from neural networks at time-series locations in the depth range 0-15 m.

Time series	TCO ₂ (μmol kg ⁻¹ year ⁻¹)		pCO ₂ (μatm year ⁻¹)	
	Measured	Computed	Measured*	Computed
BATS	1.2	1.1	1.8	1.7
HOT ALOHA SURF	1.7	1.3	1.8	1.4
ICELAND	0.9	0.9	1.5	1.6
IRMINGER	0.6	0.5	2.5	1.7

*Computed from measured A_T and TCO₂ in time series where pCO₂ was not measured.

770

Table 6: Comparison of four annual mean surface climatologies of TCO₂. Numbers in the lower-left corner represent RMSE. Numbers in the upper-right corner represent r².

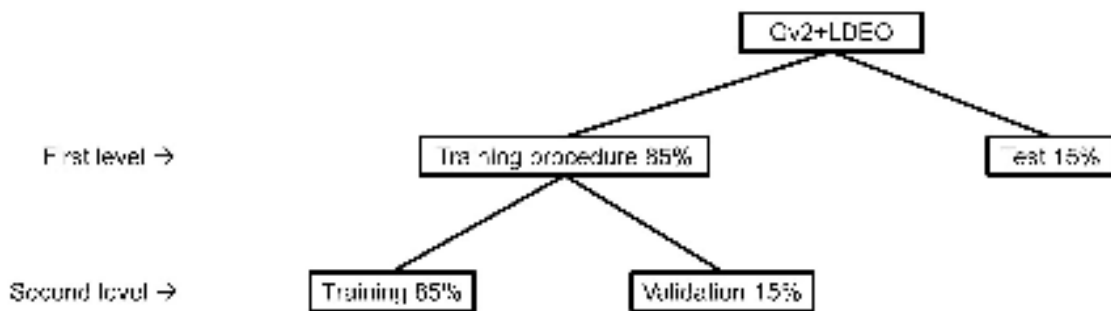
RMSE (μmol kg ⁻¹) - r ²	NNGv2LDEO	Lauvset et al. 2016*	Takahashi et al. 2014
NNGv2LDEO	-	0.93	0.97
Lauvset et al. 2016*	19.8	-	0.90
Takahashi et al. 2014	13.2	23.7	-

*The domain analyzed is the same as in Takahashi et al. (2014) for coherency reasons.

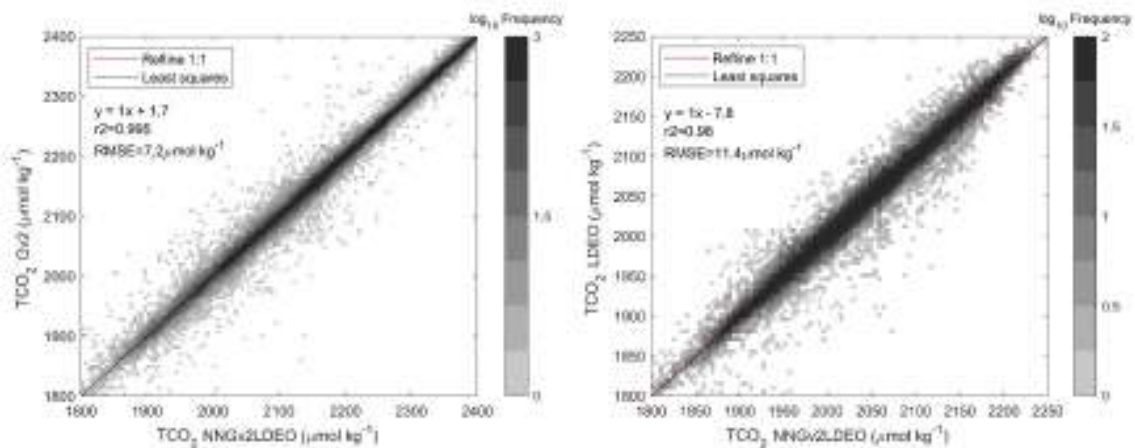
775

Table 7. Comparison of the monthly TCO₂ climatology of Takahashi et al. (2014) and the one of the present study.

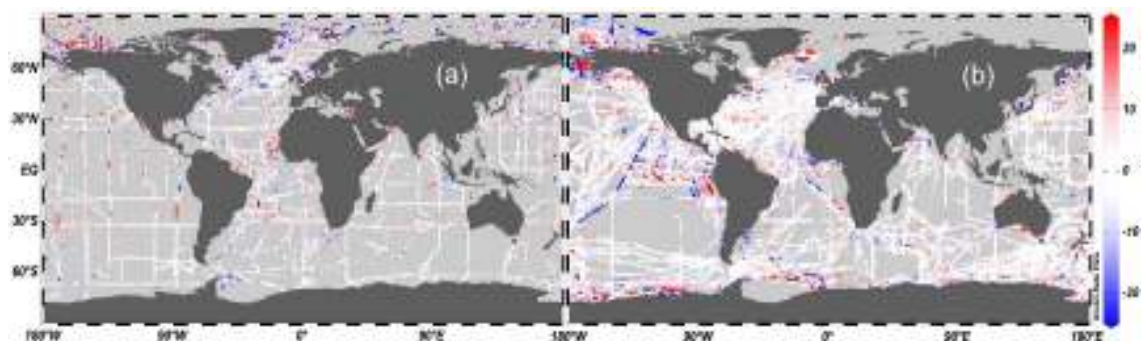
Month	RMSE (μmol kg ⁻¹)	Bias (μmol kg ⁻¹)	r ²
January	16	3.0	0.95
February	16.7	1.5	0.94
March	15.8	2.5	0.95
April	17	2.6	0.95
May	16.8	2.5	0.95
June	17.2	3.2	0.95
July	22.6	4.0	0.92
August	17.8	3.4	0.95
September	15.5	2.5	0.97
October	15.6	2.3	0.96
November	15.7	2.7	0.96
December	17.6	4.3	0.95



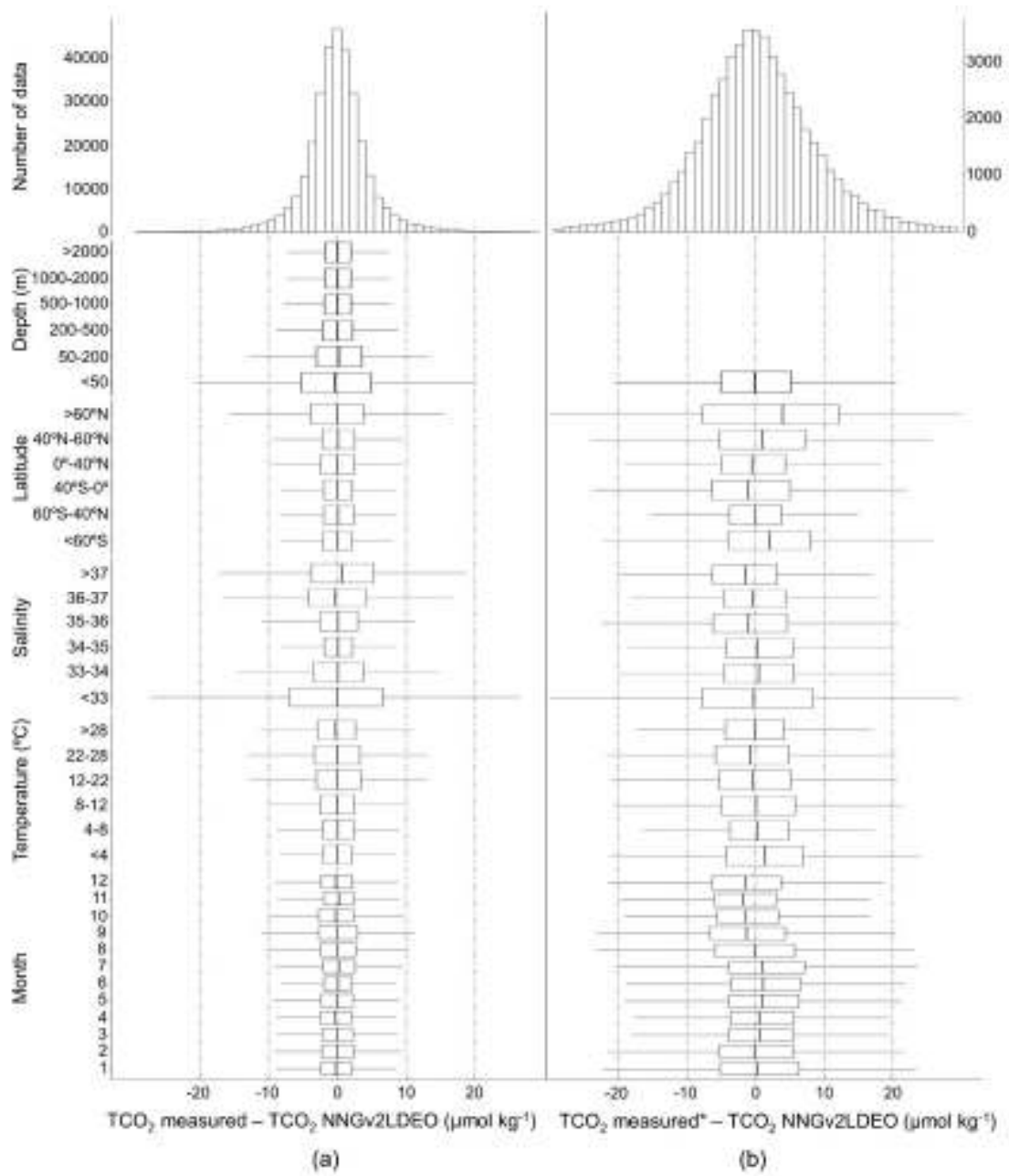
780 Figure 1. Division of the complete database in the datasets needed to train the neural network. The percentages in each level are relative to the number of data in the previous one. Data in the datasets of the first level are always the same for each network. Data in the sets of the second level are randomly associated to each set for each network to find the best network weights, because of the different starting points in the error-weight space of the training process (see also Broullón et al., 2019).



785 Figure 2. Regression of TCO₂ computed using NNGv2LDEO and TCO₂ in Gv2 and LDEO. The graph is divided in pixels. The color of each pixel is determined by the number of points inside it. Note the logarithmic scale of the pixels accounting for the large amount of data.



790 Figure 3. Differences between (a) Gv2 TCO₂ and NNGv2LDEO TCO₂ (0-30 m) and (b) LDEO TCO₂ and NNGv2LDEO TCO₂ (0 m).



795 **Figure 4. Histograms and box plots of differences between measured and neural network computed TCO₂ in (a) Gv2 and (b) LDEO. *TCO₂ computed from measured pCO₂ and neural network derived A_T.**

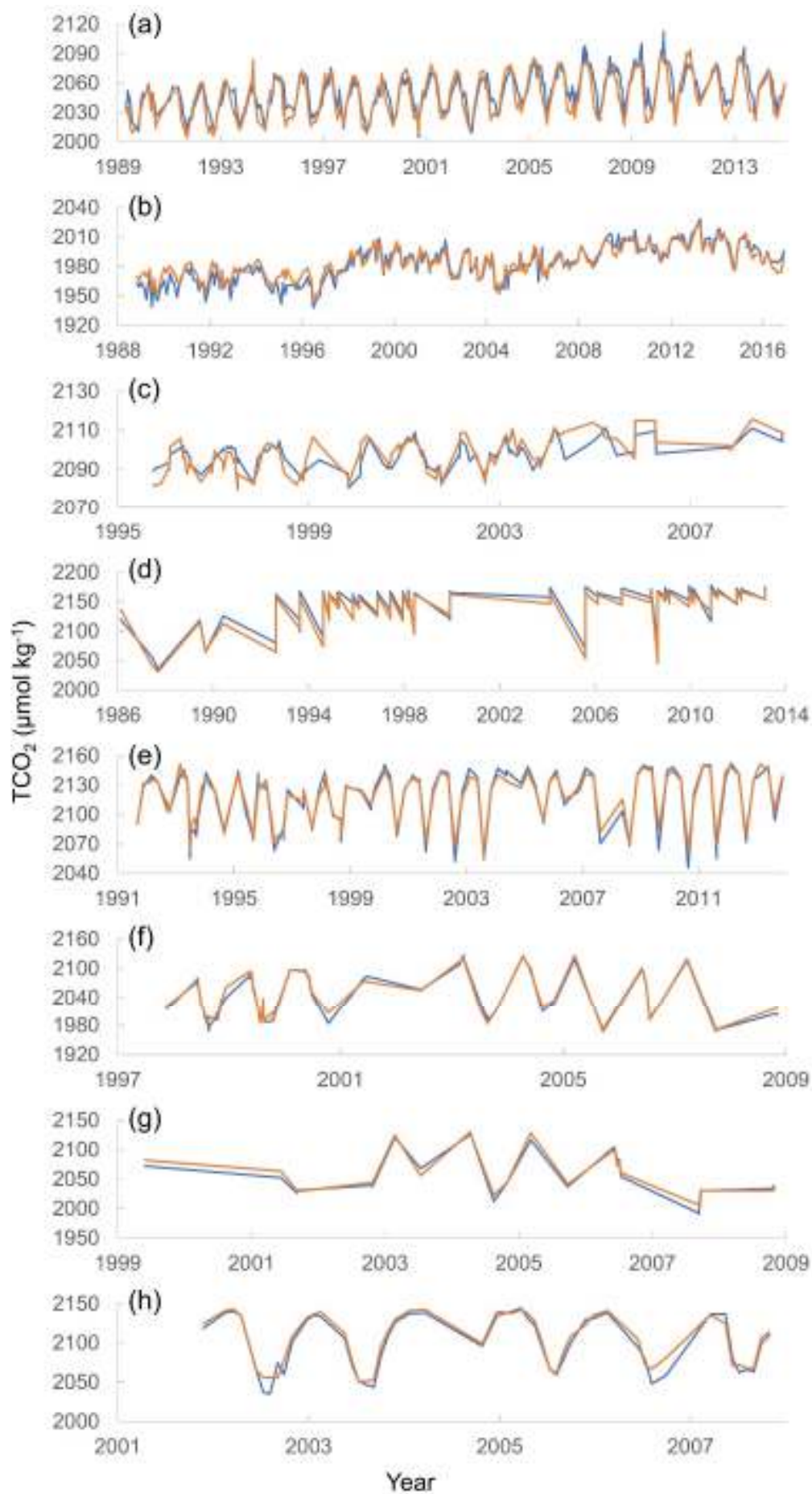
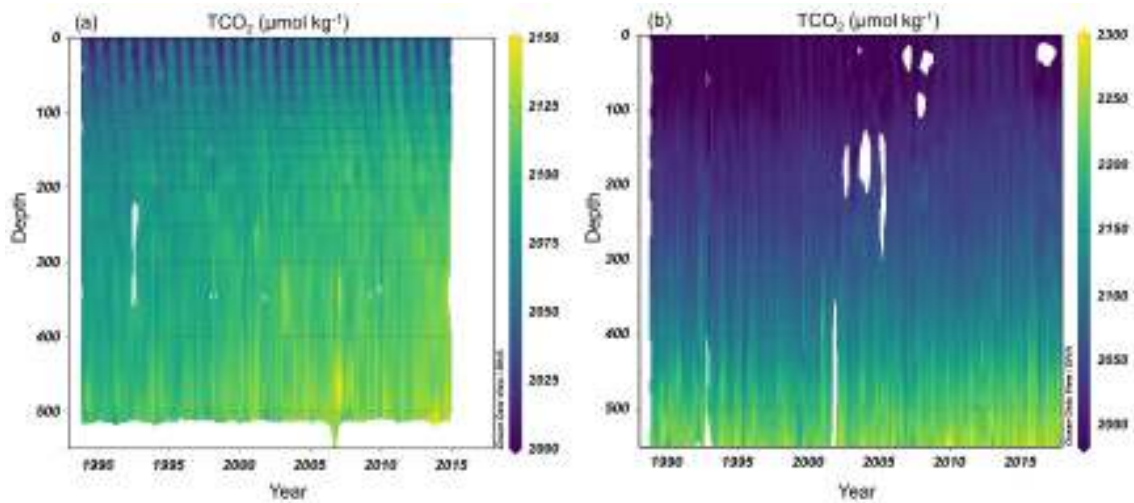
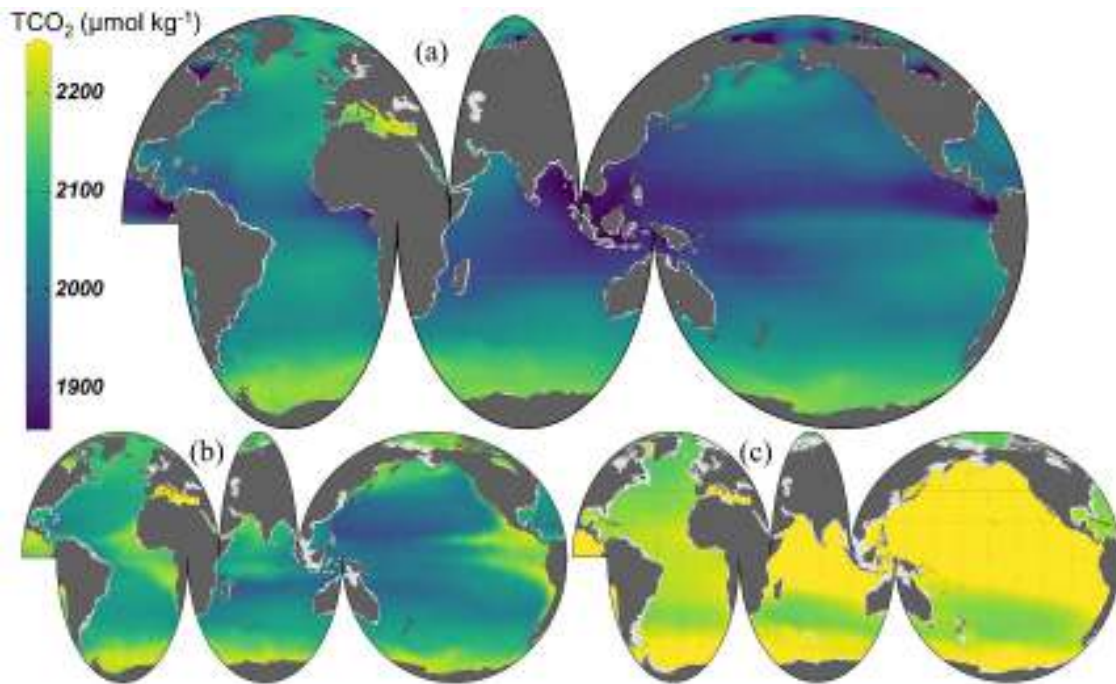


Figure 5. Measured (blue line) and computed (orange line) TCO₂ with NNGv2LDEO for the depth range 0-15 m (0-30 m in (b)) for several time series. (a) BATS, (b) HOT ALOHA SURFACE, (c) ESTOC, (d) ICELAND, (e) IRMINGER, (f) KNOT, (g) K2 and (h) OWS.



800

Figure 6. Time series of TCO₂ using NNGv2LDEO at (a) BATS and (b) HOT ALOHA locations. The water column shows a higher concentration of TCO₂ year by year. This figure was made with Ocean Data View (Schlitzer, 2016).



805

Figure 7. Annual mean climatology of TCO₂ at (a) 0 m, (b) 100 m and (c) 1000 m. This figure was made with Ocean Data View (Schlitzer, 2016).

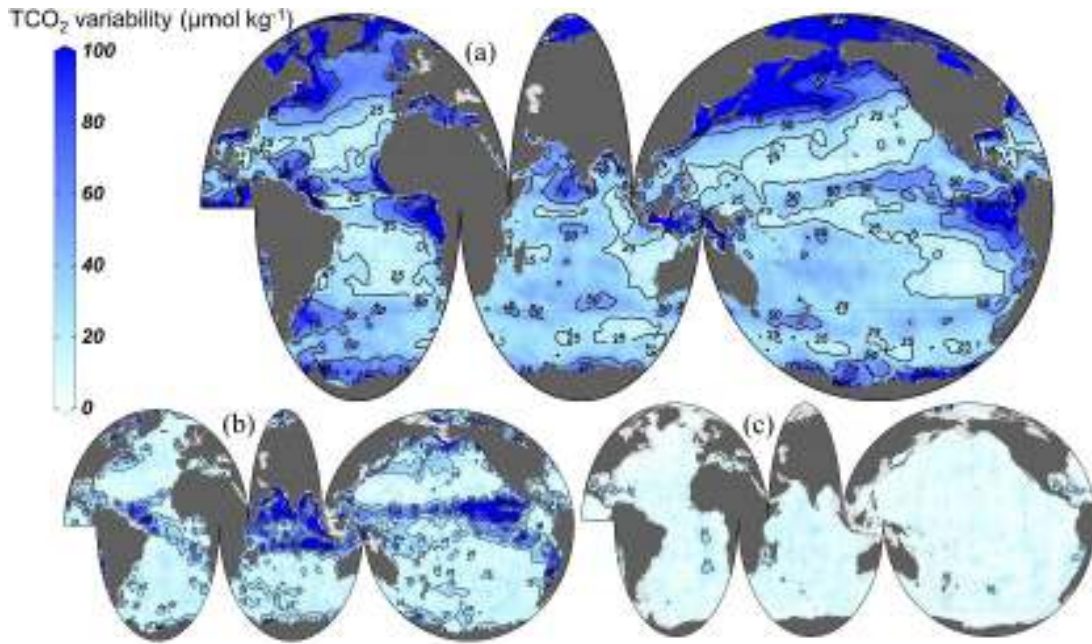
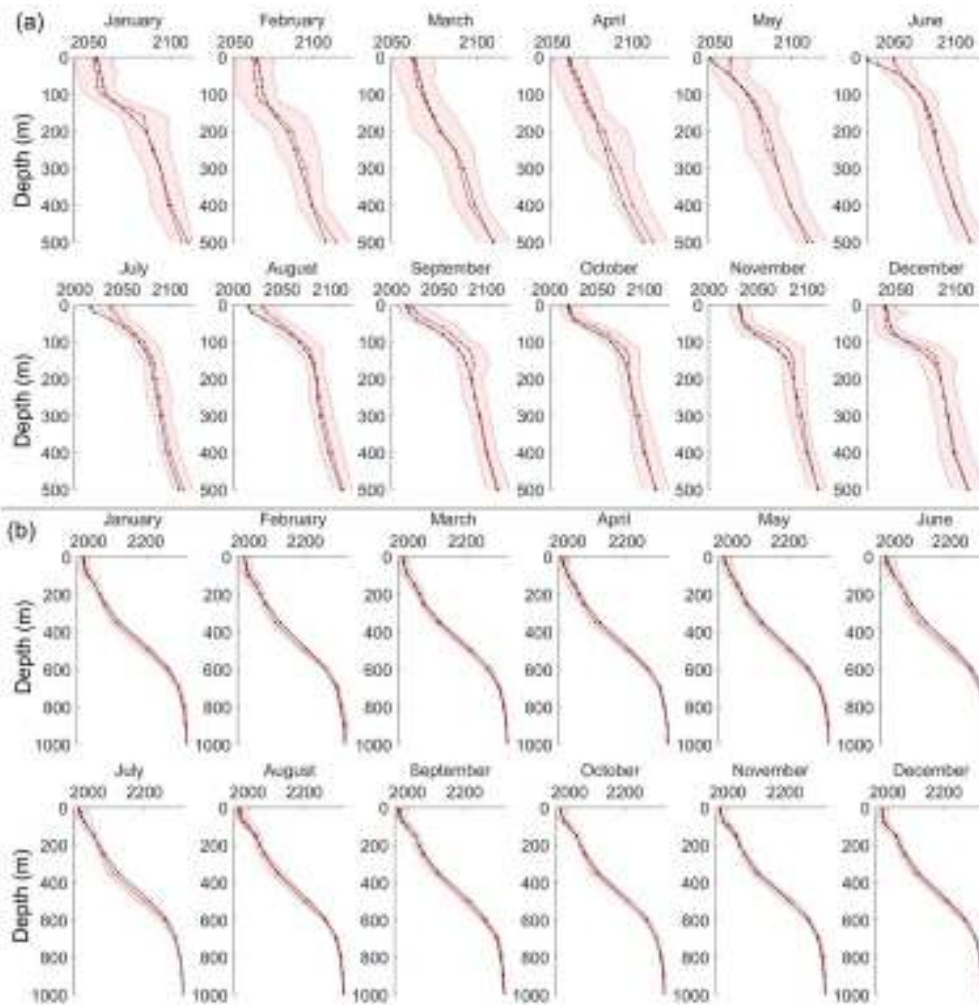


Figure 8. Seasonal amplitude of TCO₂ at (a) 0 m, (b) 100 m and (c) 1500 m. The contour lines of 25, 50, 75 and 100 μmol kg⁻¹ are shown. This figure was made with Ocean Data View (Schlitzer, 2016).



810

Figure 9. Comparison of the monthly climatological profiles of TCO₂ computed from measured data (red profile; shadow area is the standard deviation of the averaged values at each depth level) and those from the

TCO₂ climatology at (a) BATS and (b) HOT ALOHA locations. Units on the x axis are micromoles per kilogram ($\mu\text{mol kg}^{-1}$).

815

Table S1. RMSE (bias) between measured and computed TCO₂ concentrations in several time series. Units are micromole per kilogram ($\mu\text{mol kg}^{-1}$). *There is only one sample below 500 m.

Depth range	BATS	HOT ALOHA	ESTOC	ICELAND	IRMINGER	K2	KNOT	OWS	KERFIX
0-50 m	8.7 (2.7)	5.8 (-2.6)	4.4 (-0.2)	7.8 (7.1)	5.3 (-0.1)	5.3 (0.3)	8.5 (-1.3)	10.1 (-5.3)	10 (23.9)
50-200 m	7.4 (-0.3)	6.2 (0.5)	7.7 (3.9)	4.8 (7.5)	4.9 (4.9)	3.6 (1.4)	5.4 (-0.9)	7.3 (-1.2)	10 (26.4)
200-500 m	6.1 (-1.8)	4.2 (0.9)	5.9 (1.9)	3.1 (6.2)	3.2 (5)	2.6 (1.2)	6 (-1.1)	3.9 (-1)	19.2 (28.8)
>500 m	6.4 (-2.7)	3.8 (-1.6)	6.6 (-0.6)	3.4 (3.3)	3.5 (5.5)	2.1 (1.7)	4.1 (-0.4)	3.1 (1.9)	-*

Table S2. Comparison between the TCO₂ climatology of Lauvset et al. (2016) and the one of the present study at different depth levels.

Depth layer	RMSE ($\mu\text{mol kg}^{-1}$)	Bias ($\mu\text{mol kg}^{-1}$)	r ²
0	31.5	-8.3	0.85
100	15.9	0.9	0.95
250	10.5	1.3	0.97
500	7.6	1.0	0.99
1000	6.8	0.4	0.99
2000	4.8	-0.4	0.995
3000	5.3	-1.4	0.993
4000	5.4	-1.2	0.99

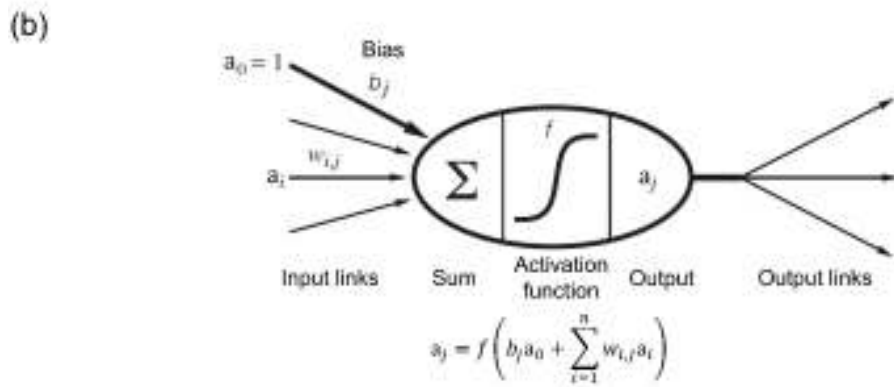
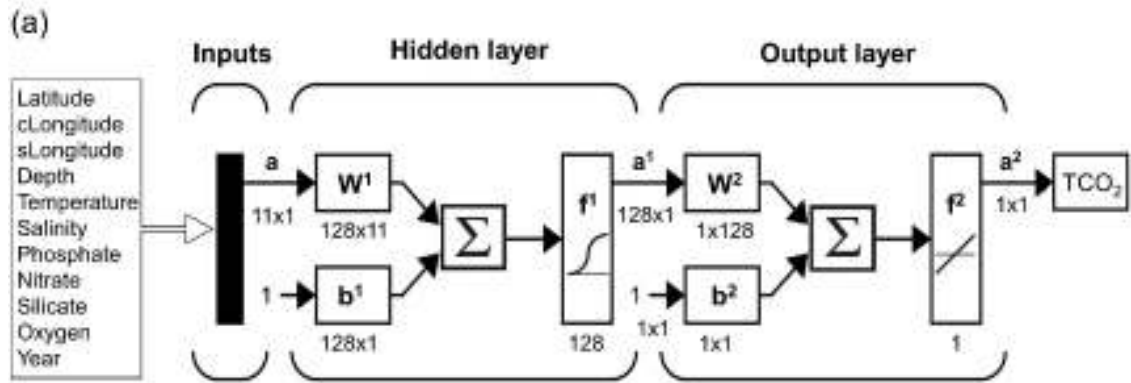


Figure S1. (a) Neural network configuration. The notation is in agreement with Hagan et al. (2014). \mathbf{a} : input vectors; \mathbf{W} : weight matrix; \mathbf{b} : bias matrix; Σ : sum; f : transfer function; \mathbf{a}^X : output matrix. The superscripts indicate the number of the layer. $cLongitude = \cos(\frac{\pi}{180^\circ} longitude)$; $sLongitude = \sin(\frac{\pi}{180^\circ} longitude)$. The dimensions of the matrices are for an individual sample. Modified from Hagan et al. (2014). (b) Neuron. a_i : inputs to each neuron; $w_{i,j}$: weights of each input to each neuron. Modified from Russell and Norvig et al. (2010).

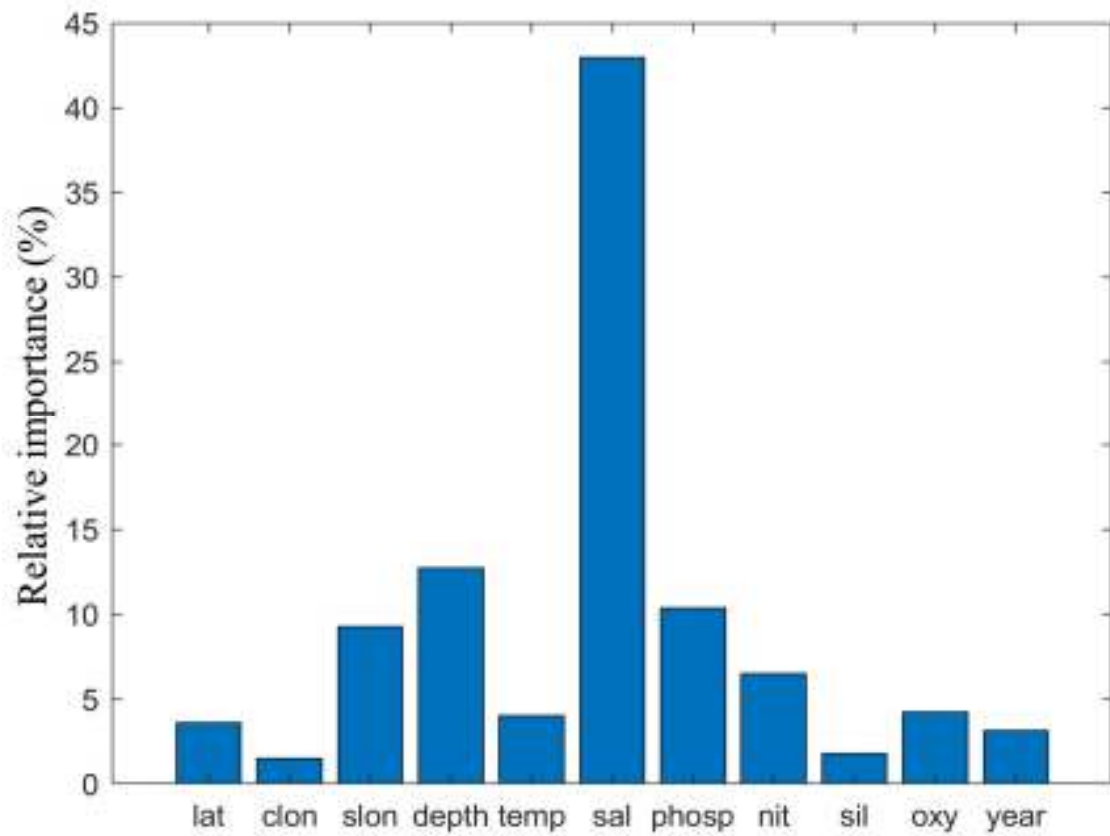


Figure S2. The relative importance of the input variables for NNGv2LDEO obtained with Eq. (1). lat: latitude; clon: clongitude; slon: slongitude; temp: temperature; sal: salinity; phosp: phosphate; nit: nitrate; sil: silicate; oxy: oxygen.

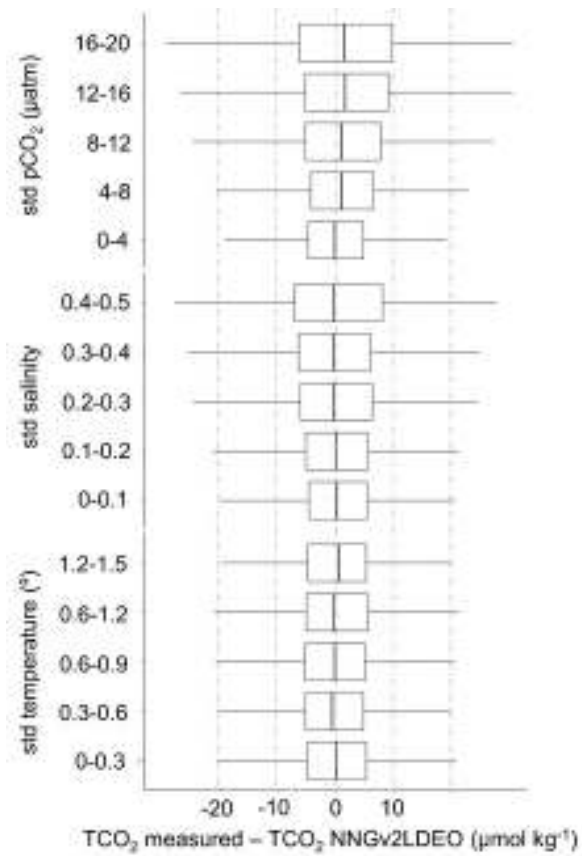


Figure S3. Box plots of differences between measured and computed TCO₂ in LDEO by standard deviation (std) ranges obtained from the monthly average of the LDEO data.

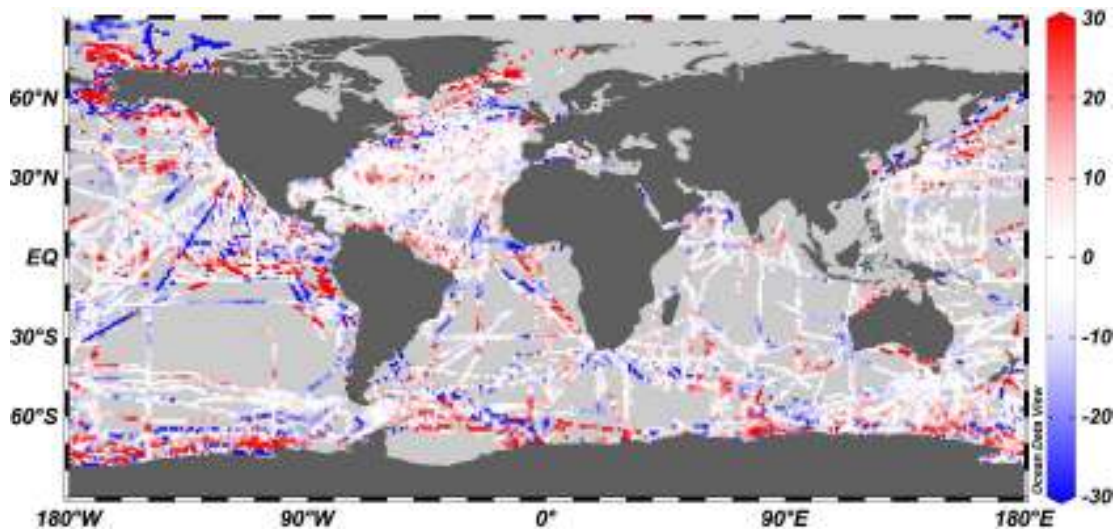


Figure S4. Differences between measured and computed pCO₂ with Ar from NNGv2 (Broullón et al., 2019) and TCO₂ from NNGv2LDEO in LDEO. Units are microatmospheres (µatm).

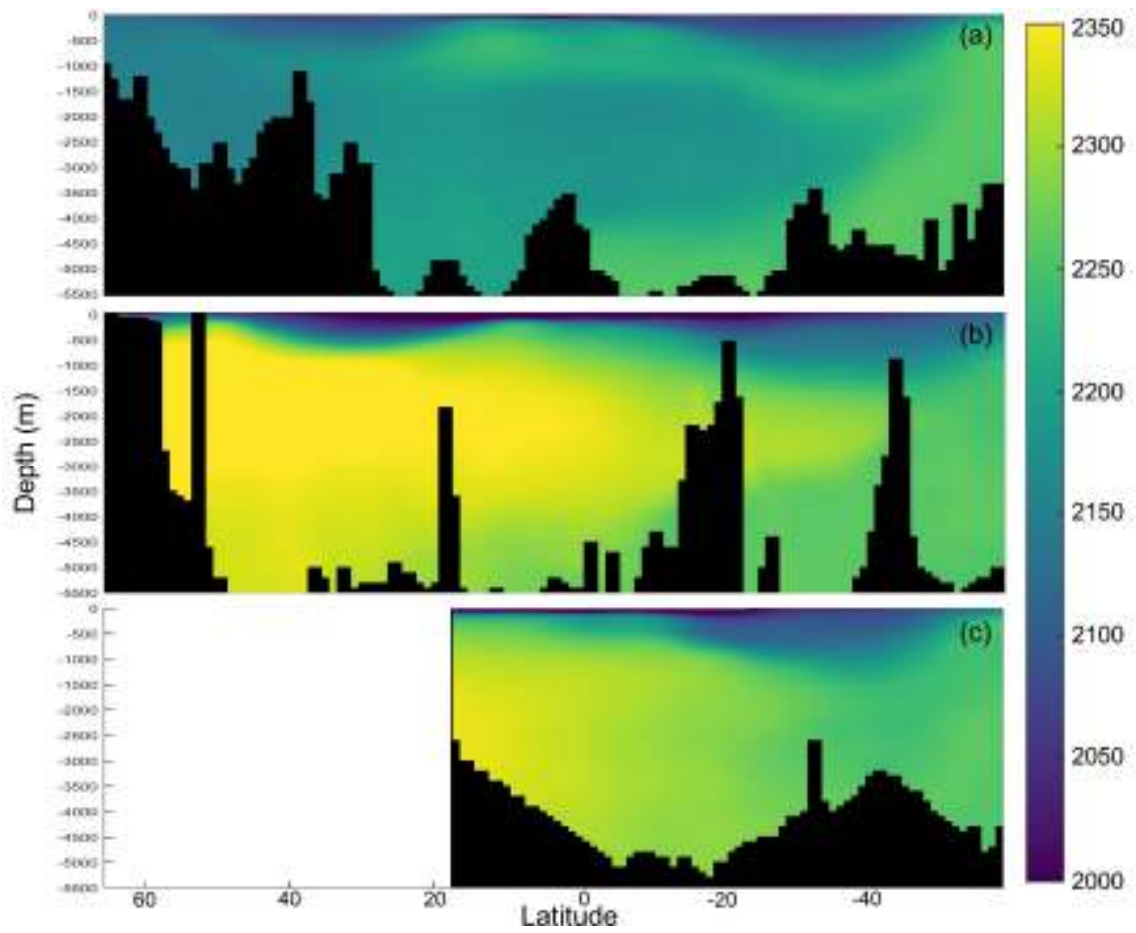


Figure S5. Sections of TCO₂ in (a) Atlantic (longitude: 28.5° W), (b) Pacific (longitude: 174.5° W) and (c) Indian (longitude: 84.5° E) oceans. Units are micromole per kilogram (μmol kg⁻¹).

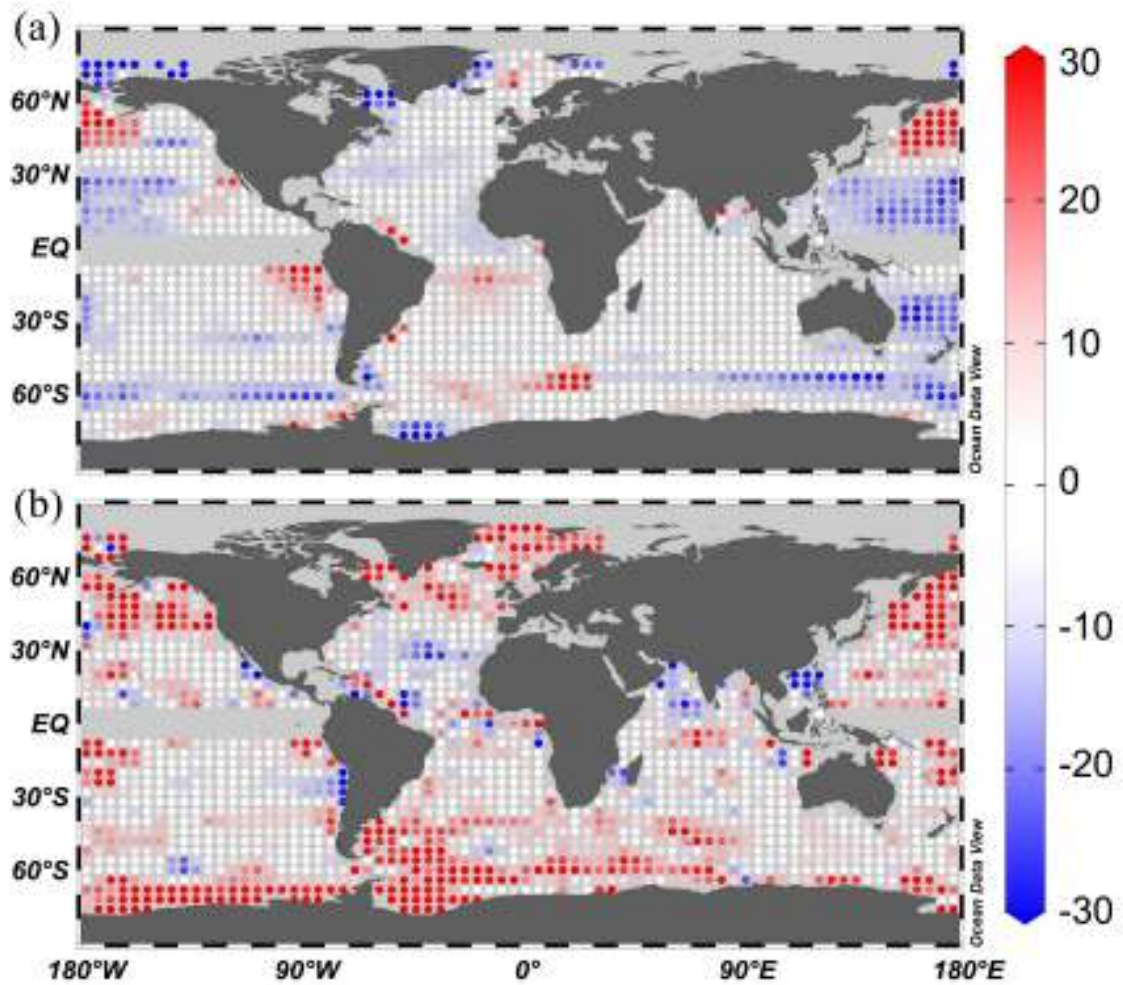


Figure S6. Differences between the annual mean of surface TCO₂ neural network climatology and (a) Takahashi et al. (2014) and (b) Lauvset et al. (2016) surface annual mean climatology. Units are micromole per kilogram ($\mu\text{mol kg}^{-1}$). The color bar was developed in order to show the highest differences beyond the errors of each method. This figure was made with Ocean Data View (Schlitzer, 2016).

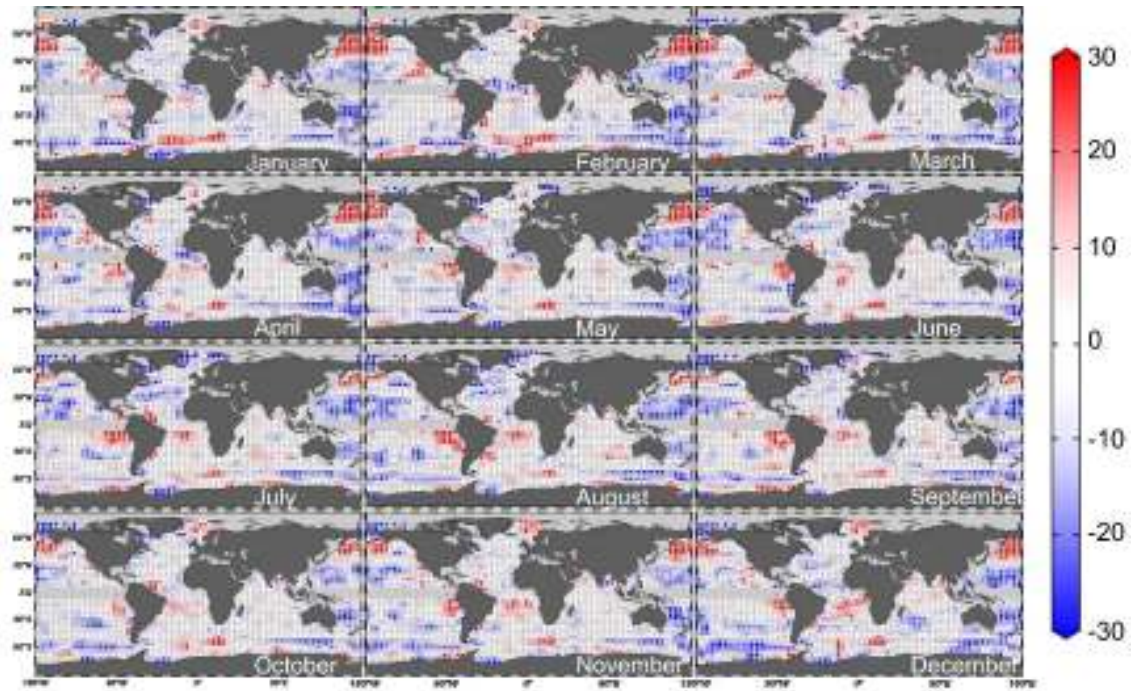


Figure S7. Differences between the monthly climatology of TCO₂ of Takahashi et al. (2014) and the one of the present study. The color bar was developed in order to show the highest differences beyond the errors of each method. Units are micromole per kilogram ($\mu\text{mol kg}^{-1}$). This figure was made with Ocean Data View (Schlitzer, 2016).

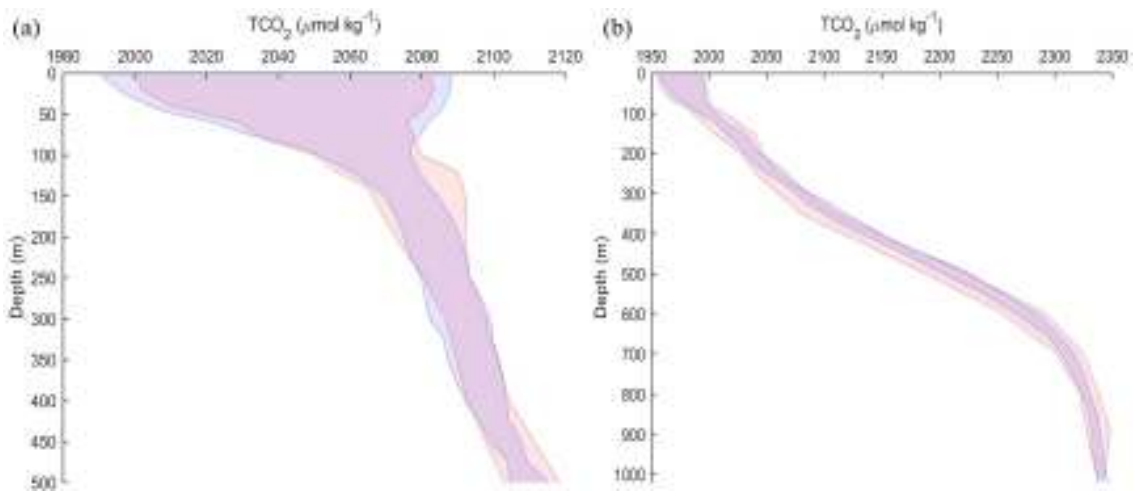


Figure S8. Profiles of the seasonal variability of the measured data (red lines and red shadow) and the TCO₂ climatology (blue lines and blue shadow) at (a) BATS and (b) HOT ALOHA locations. The variability of the measured data was computed subtracting the maximum and the minimum TCO₂ values of the measured climatological profiles depicted in Fig. 9. Note the different color of the overlapped area.

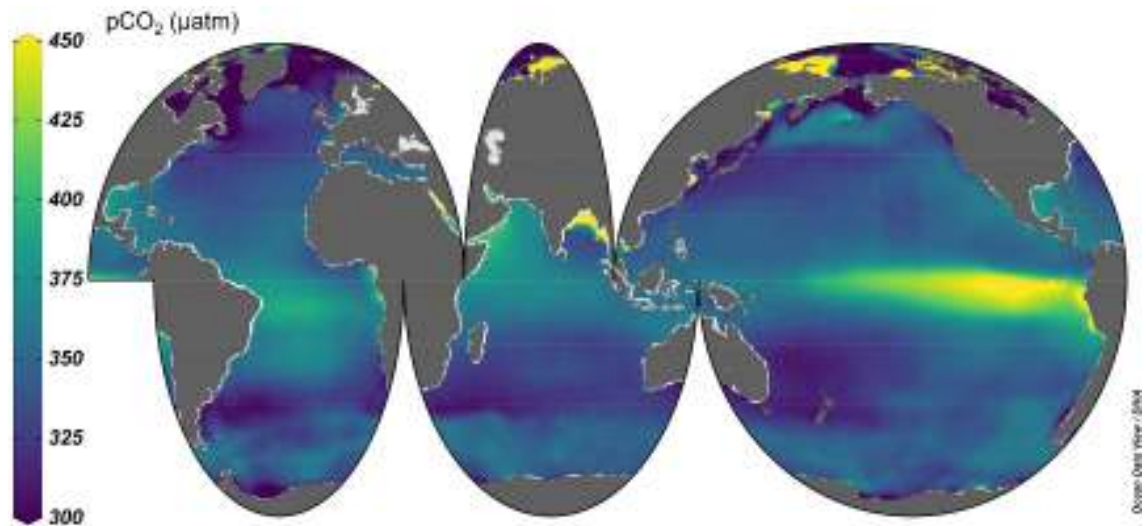


Figure S9. Annual mean $p\text{CO}_2$ centered in 1995 computed from the annual mean A_T (Broullón et al., 2019) and TCO_2 (this study). It should be noted that the extremely high values in the coastal waters of the Arctic Ocean are derived from a TCO_2/A_T ratio higher than 1. This fact is determined by the difficulty of neural networks to model both variables under the influence of river discharges with high concentrations of A_T and TCO_2 , but TCO_2/A_T ratios higher than 1 are also found in the Arctic Ocean for the measured data in GLODAPv2.2019 (Olsen et al., 2019).

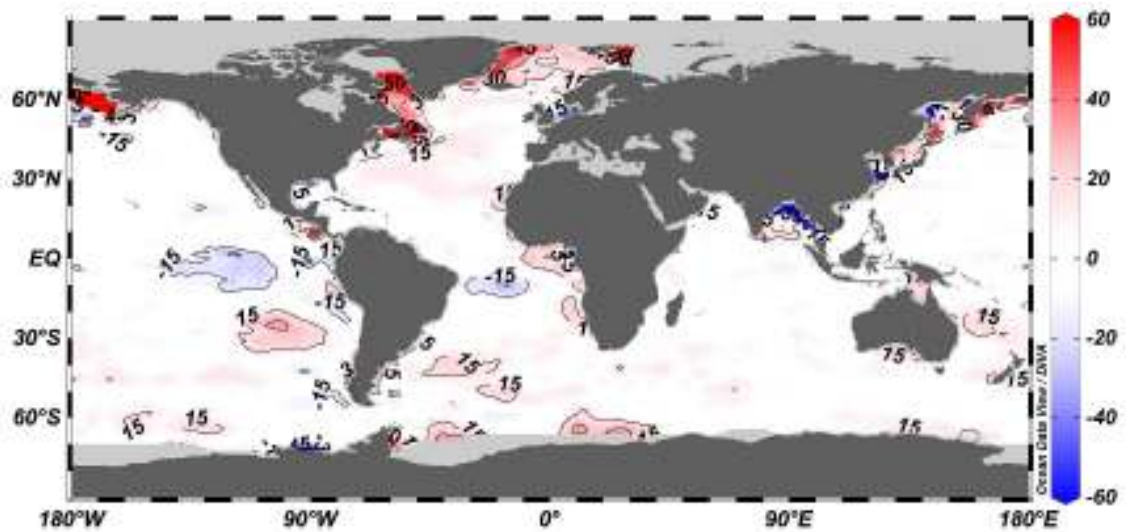


Figure S10. Differences between the annual mean climatology of $p\text{CO}_2$ from Landschützer et al. (2017) centered in 1995 and the one computed in the present study. Units are microatmospheres (μatm). The contour lines of 15, 30, 45 and 60 μatm are shown. This figure was made with Ocean Data View (Schlitzer, 2016).

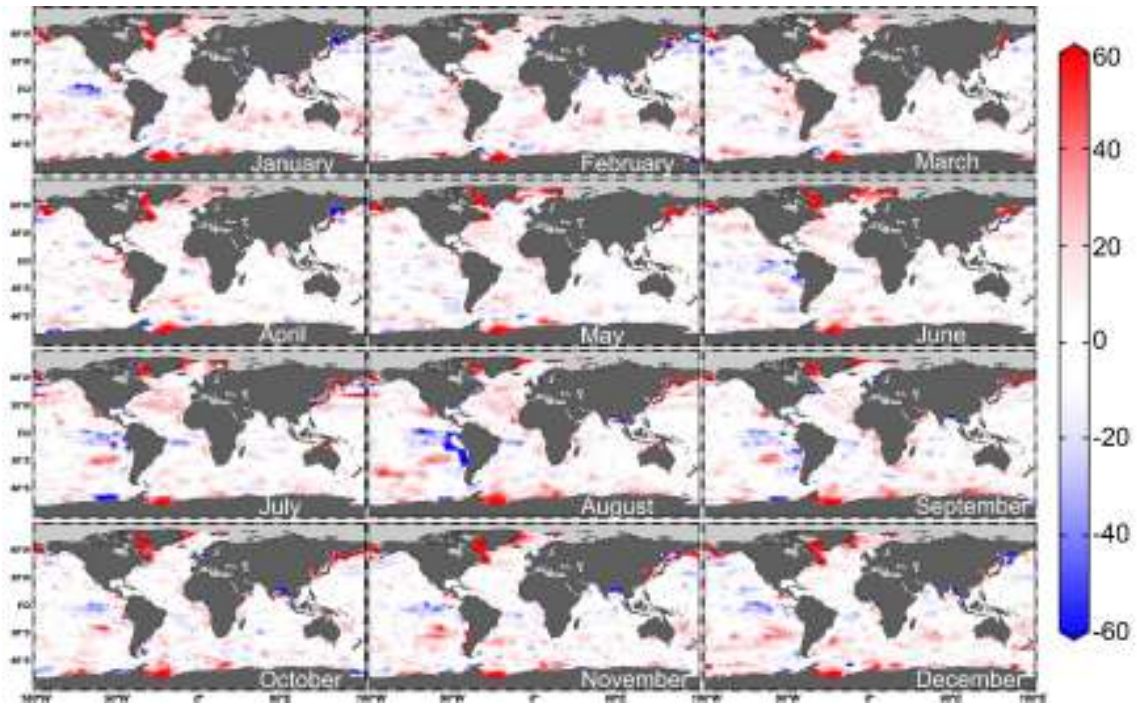


Figure S11. Differences between the monthly climatology of pCO₂ from Landschützer et al. (2017) centered in 1995 and the one computed in the present study. Units are microatmospheres (μatm). The contour lines of 15, 30, 45 and 60 μatm are shown. This figure was made with Ocean Data View (Schlitzer, 2016).

pCO₂ variability (μatm)

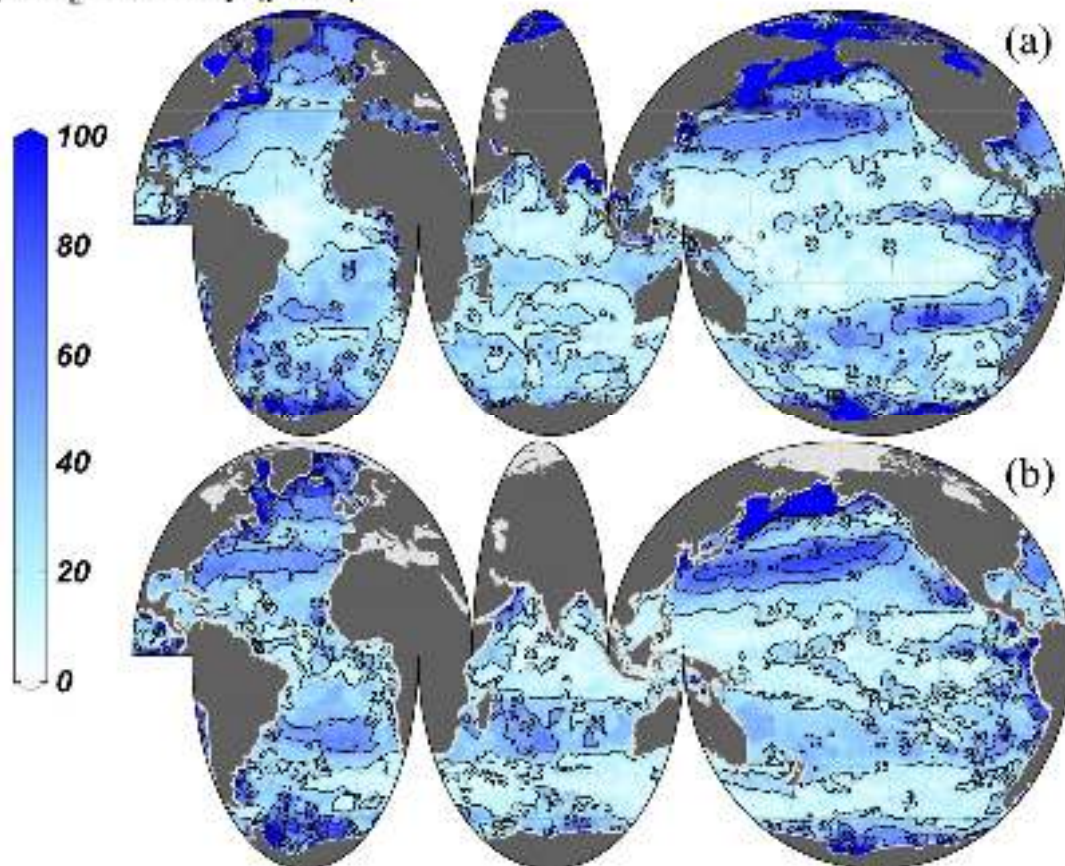


Figure S12. Seasonal amplitude of surface pCO₂ of (a) this study and (b) Landschützer et al. (2017) centered in the year 1995. The contour lines of 25, 50, 75 and 100 μatm are shown. This figure was made with Ocean Data View (Schlitzer, 2016).

References

Broullón, D., Pérez, F. F., Velo, A., Hoppema, M., Olsen, A., Takahashi, T., Key, R. M., Tanhua, T., González-Dávila, M., Jeansson, E., Kozyr, A. and van Heuven, S. M. A. C.: A global monthly climatology of total alkalinity: a neural network approach, *Earth Syst. Sci. Data*, 11(3), 1109–1127, doi:10.5194/essd-11-1109-2019, 2019.

Hagan, M. T., Demuth, H. B., Beale, M. H., and De Jesus, O.: *Neural network design*, ISBN 978-0971732117, available at: <http://hagan.okstate.edu/nnd.html> (last access: 26 July 2018), 2014.

Landschützer, P., Gruber, N. and Bakker, D.C.E.: An updated observation-based global monthly gridded sea surface pCO₂ and air-sea CO₂ flux product from 1982 through 2015 and its monthly climatology (NCEI Accession 0160558). Version 2.2. NOAA National Centers for Environmental Information. Dataset. [2017-07-11], (last access: 15 July 2019), 2017

Lauvset, S. K., Key, R. M., Olsen, A., Van Heuven, S., Velo, A., Lin, X., Schirnack, C., Kozyr, A., Tanhua, T., Hoppema, M., Jutterström, S., Steinfeldt, R., Jeansson, E., Ishii, M., Perez, F. F., Suzuki, T. and Watelet, S.: A new global interior ocean mapped climatology: The 1° × 1° GLODAP version 2, *Earth Syst. Sci. Data*, 8(2), 325–340, doi:10.5194/essd-8-325-2016, 2016.

Russell, S. J. and Norvig, P.: *Artificial intelligence: a modern approach*, Prentice Hall, 2010.

Schlitzer, R., *Ocean Data View*, available at: <http://odv.awi.de> (last access: 21 May 2018), 2016.